Thin-Film Photovoltaics Partnership Program

Special Report – Year II

Deliverable **D.2.6**: Subcontract ADJ-2-30630-13

Project: **Fundamental Materials Research and Advanced Process Development for Thin-Film CIS-Based Photovoltaics**

P.I.: T. J. Anderson

Co-PI's: Sheng S. Li , Oscar D. Crisalle, and Valentin Craciun

Other Personnel: Ryan Kaczynski, Woo Kyoung Kim, and Seokhyun Yoon

Subcontract No.: ADJ-2-30630-13

Funding Agency: National Renewal Energy Laboratory (NREL)

Program: Thin-Film Photovoltaics Partnership program

Contact Address: Tim Anderson, P.O. Box 116005, 227 Chemical Engineering Bldg., University of Florida, Gainesville FL 32611-6005, Phone: (352) 392-0882, FAX: (352) 392-9513, E-mail: tim@nersp.nerdc.ufl.edu

Study of Grain Boundary Effects in CIS Solar Cells

A Special Report

1.1 Introduction

Thin-film layers of CIGS (cupper-indium-gallium-diselenide) are polycrystalline materials with an average grain size on the order of a several microns. The relatively high density of grain boundaries and the associated trap states at those boundaries would be expected to adversely influence device performance. It has been puzzling then that high-efficiency cells (as high as 19.2% [1-1]) have been demonstrated using polycrystalline material, while such high efficiencies are actually to be anticipated to be realized with grain-free single-crystal absorbers in the case of Si solar cells. The question that arises naturally is: what is the role of grain-boundaries in the enhancement of device performance?

This report investigates the effects that CIS grain boundaries have on the device performance of solar cells having a structure that can be described via the following succinct notation: /ZnO/CdS/CIS/Mo-glass. The approach consists of carrying out one-dimensional and two-dimensional device simulation studies using the commercially available semiconductor-simulation package *Taurus Medici* [www.synopsis.com] that models the electrical, thermal, and optical characteristics of semiconductor devices.

1.2 Electrostatics of the p-n Junction in Solar Cells

A solar cell is a minority-carrier device. Since the scope of this study is limited to the absorber layer of thin-film CIS solar cells, only the electrostatics of the p-type absorber layer is reviewed. The transport of charged carriers in the absorber layer is described by Poisson's equation and the carrier continuity equations, as follows:

$$\rho = \varepsilon \nabla E = \varepsilon \nabla \bullet (-\nabla V) = -\varepsilon \nabla^2 V = q(p - n + N_D - N_A) \tag{1-1}$$

$$\frac{\partial n}{\partial t} = \frac{1}{q}\nabla \bullet J_N - U_N + G_L, \quad where \quad J_N = q\mu_N nE + qD_N \nabla n \tag{1-2}$$

$$\frac{\partial p}{\partial t} = -\frac{1}{q}\nabla \bullet J_P - U_P + G_L, \quad where \quad J_P = q\mu_P pE - qD_P \nabla p \tag{1-3}$$

where ρ, ε, E, and V are the charge density, dielectric constant, electric field, and the electric potential, respectively. Also, the variables p, n, N_D and N_a represent the hole density, electron density, and doping density of donors and of acceptors. Equations (1-2) and (1-3) are respectively known as the carrier continuity equations for holes and electrons, where *q* is the electronic charge, J_P and J_N are the hole and electron current-density vectors that contain both drift and diffusion terms, U_i is the recombination rate for carrier i, and G_L is the generation rate of an equal number of holes and electrons by light injection. In the carrier continuity equations, the recombination rate U can be represented as the sum of the band-to-band recombination, Auger recombination, and Shockley-Read-Hall (SRH) recombination [1-2]. The band-to-band recombination refers to the recombination between the electrons at the conduction band and the

holes in the valence band. In Auger recombination, electrons in the conduction band first lose their energy by collision with the other electrons, and then recombine with the holes in the valence band. SRH recombination is a recombination process where one or both carriers pass through states with energy levels in the bandgap. Usually, the band-to-band recombination as well as the Auger recombination terms are neglected, because they are small compared to the SRH recombination term. The rate of SRH recombination through a single trap can be represented by the equation

$$U = U_{SRH} = \frac{pn - n_i^2}{\tau_p[n + n_i \exp(\frac{E_{trap}}{kT})] + \tau_n[p + n_i \exp(\frac{-E_{trap}}{kT})]}, \qquad (1\text{-}4)$$

$$where \quad E_{trap} = E_t - E_i$$

and where n_i is the intrinsic carrier concentration, and E_{trap} is the energy difference between the trap state level and the midgap level. The variable τ_i is the lifetime of carrier type I, and it can be either constant or carrier-concentration dependent. If the trap state in the gap acts as a trap for an electron or hole, in addition to serving as a recombination center, Poisson's equation should be modified since such traps add to the net charge distribution. First, the probability f_i of filling trap state i for an electron or hole is given as follows:

$$f_i^{electron} = \frac{\tau_{pi} n + \tau_{ni} p_{ti}}{\tau_{pi}(n + n_{ti}) + \tau_{ni}(p + p_{ti})} \qquad (1\text{-}5)$$

$$f_i^{hole} = \frac{\tau_{pi} n_{ti} + \tau_{ni} p}{\tau_{pi}(n + n_{ti}) + \tau_{ni}(p + p_{ti})} \qquad (1\text{-}6)$$

where τ_{pi} and τ_{ni} are the carrier lifetimes at trap state i, and p_{ti} and n_{ti} are the carrier concentrations at the trap states. For hole traps, Poisson's equation is be modified to adopt the form

$$-\varepsilon \nabla^2 V = q(p - n + N_D - N_A + \sum_i N_{ti} f_i^{hole}) \qquad (1\text{-}7)$$

Furthermore, if the trap state acts as donor state or acceptor state with a very shallow energy level, Equation (1-7) must be modified to adopt the forms:

$$-\varepsilon \nabla^2 V = q(p - n + N_D - N_A - \sum_i N_{ti}(f_i - 1)) \quad \text{for the donor state} \qquad (1\text{-}8)$$

$$-\varepsilon \nabla^2 V = q(p - n + N_D - N_A + \sum_i N_{ti}(f_i - 1)) \quad \text{for the acceptor state} \qquad (1\text{-}9)$$

In solar cells, the generation term, G_L in Equations (1-2) and (1-3) corresponds to photogeneration by sun light, namely, the generation of the electron-hole pairs when the energy

of the photons is larger than the bandgap of the absorber layer, and it is defined by the following equation for the one-dimensional case:

$$G(x) = \int_{\nu_1}^{\nu_2} G(x,\nu)d\nu = \int_{\nu_1}^{\nu_2} \beta(\nu)\alpha(\nu)S_0(\nu)(1-R)\exp(-\alpha(\nu)x)d\nu \tag{1-10}$$

where R is the reflectivity and β is the quantum efficiency that takes into account that only a fraction of the absorbed photons generates electron-hole pairs. The variable α is the absorption coefficient, and S_0 is the incident photon flux per unit area, both of which are dependent on the frequency of the incident light. Therefore, the photogeneration term can be calculated if the spectrum of the impinging light and the absorption properties of the absorber layer are known.

Given information about the generation and recombination terms, the continuity and Poisson's equation, along with appropriate boundary conditions, can be solved for five specified layers of the solar cell device. For an ideal p-n junction solar cell with no series resistance and infinite shunt resistance, the total current is represented as the following well-known current-voltage characteristic expression obtained from the solution of the previous equations [1-3]:

$$I = I_0\{\exp(\frac{qV}{kT}) - 1\} - I_L \tag{1-11}$$

where I_L is the photo-current by light injection, and the saturation current I_0 is given by

$$I_0 = qA\{\frac{D_n n_i^2}{L_n N_A} + \frac{D_p n_i^2}{L_p N_D}\} \tag{1-12}$$

This relationship assumes there is no recombination at the front and back surfaces. Considering the recombination of the carriers by SRH recombination at the trap states near the midgap, which gives the maximum recombination rate, the recombination current should be added to the photo-generation current in Equation (1-11), which leads to the equation

$$I = I_0\{\exp(\frac{qV}{kT}) - 1\} - I_L + I_{SRH} = I_0\{\exp(\frac{qV}{kT}) - 1\} - I_L + I_{SRH0}\{\exp(\frac{qV}{2kT}) - 1\},$$
$$with \quad I_{SRH0} = \frac{qAWn_i}{2(\tau_{p0} + \tau_{n0})} \tag{1-13}$$

where I_{SRH0} is the reverse saturation current by SRH recombination, W is the width of the depletion region, n_i is the intrinsic carrier density and τ_{i0} is the carrier lifetime for each carrier type.

The current-voltage characteristics of p-n junction solar cells, however, should be further further because there are other parameters of relevance, such as series resistance, R_s, and shunt resistance, R_{sh}. The series resistance includes the bulk resistance of the semiconductor as well as the resistance of the contacts and interconnections. The origins of the shunt resistance are related to the lattice defects, such as grain boundaries or large precipitates. The equivalent electrical

circuit of a p-n junction solar cell is drawn in Figure 1-1, where I_0 is the diffusion current and I_{SRH} is the SRH recombination current. The total current including the series and shunt resistances can be represented by

$$I = I_0\{\exp(\frac{q(V-IR_s)}{kT})-1\} + I_{SRH0}\{\exp(\frac{q(V-IR_s)}{2kT})-1\} + \frac{(V-IR_s)}{R_{sh}} - I_L \tag{1-14}$$

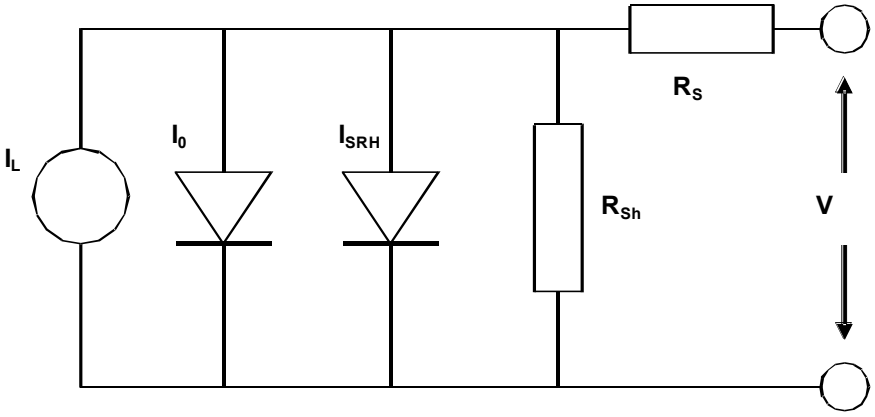

Figure 1-1. Equivalent circuit of a p-n junction solar cell.

In the theory of the device physics of solar cells, two important characteristics are the *short circuit current* J_{SC}, (i.e., the current when V = 0), and the *open-circuit voltage*, V_{OC}, (i.e., the voltage when I = 0). Analytical expressions for I_{SC} and V_{OC} can be obtained for ideal conditions. For example, from Equation (1-14), the short circuit current is equal to the light-generated current I_L only if R_s is equal to zero. In a similar vein, the following analytical expression can be obtained for the open circuit voltage when $R_s = 0$, $R_{sh} = \infty$ and $I_{SRH} = 0$:

$$V_{OC} = \frac{kT}{q}\ln\{\frac{I_L}{I_0}+1\}$$

The ensuing sections make use of general-purpose device simulation software package TAURUS MEDICI to simulate the effect of grain boundaries on the device performance. Developed by Avant! Co. and marketed by Synopsis [www.synopsis.com], the software tool has a capability of carrying out one- or two-dimensional simulation studies with the consideration of SRH, band-to-band, and Auger recombination.

1.3 One-Dimensional Simulation Study

This section presents one-dimensional simulations performed to validate the codes by ensuring that the results are physically reasonable via comparison with a few well known cases. The layer structure /ZnO(transparent conducting oxide)/ZnO(n-type)/CdS(n-type)/CIS(p-type)/Mo/ was used to represent the solar cell for the simulation. The front and back contacts, namely ZnO and Mo, were assumed to be ohmic, each with a potential equal to the applied bias (Dirichlet boundary condition). The film thickness and other physical properties of each layer

are summarized in Table 1-1.

Table 1-1. Electrical properties of each layer in the simulated device.

Layer	Thickness (nm)	Doping (cm^{-3})	E_G (eV)	ε (F/cm)	χ (eV)
CIS	2000	8×10^{16}	1.04	13.6	3.8
CdS	30	6×10^{16}	2.4	10	3.75
ZnO	50	5×10^{17}	3.3	9	4.0

To properly account for the photo-generation of carriers, the spectral distribution of incident solar energy must be properly taken into consideration. The solar spectrum depends on the extent of air absorption that occurs before impinging the surface of the solar cell. The standard AM0 indicates that there is no air in the light path (i.e., extraterrestrial space). Nonzero values of air mass are defined by the relationship (AM value) = 1/cos(Z), where Z is the angle between the sun light and the normal of the earth's surface. Therefore, AM1 represents sun light that is impinging the surface with an angle of 90°. In this study, the solar spectrum used is the spectrum for blackbody radiation at 5800 K, which corresponds to the AM0 condition (See Figure 1-2).

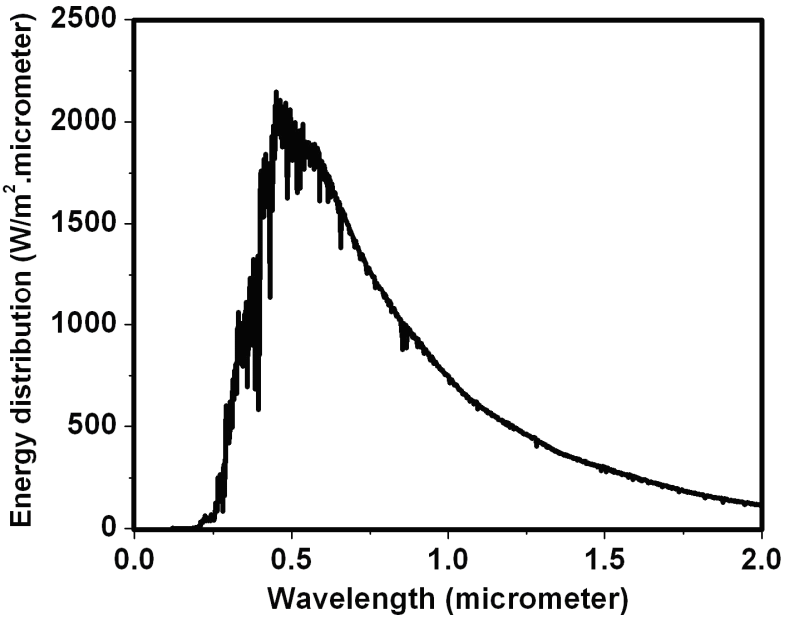

Figure 1-2. Solar spectrum for AM0 condition.

The absorption coefficient utilized for each semiconductor layer (ZnO, CdS and CIS) is shown in Figure 1-3. As can be seen, the absorption coefficient decreases rapidly as the wavelength becomes greater than the value corresponding to the bandgap energy of the semiconductor.

The doping of the CIS layer was defined by acceptor states with a density of 8×10^{16} cm^{-3}, located 80 meV above the valence band, and with a carrier lifetime of 10^{-6} s both for electrons

and holes. These values were selected to show the effect of the other parameters, such as deeper acceptor level and compensating donors. The device model also requires the values of the electron affinity χ, and dielectric constant ε.

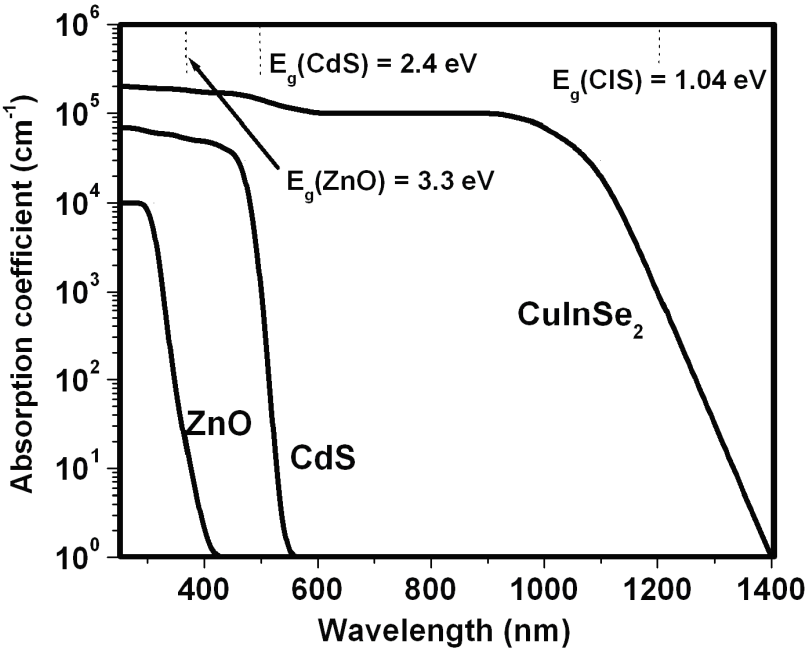

Figure 1-3. Absorption coefficient of each semiconductor layer in the device model.

1.3.1 Reference Case

The current-continuity and Poisson's equations are solved for this case without any recombination center and trap states included in the device model. The resulting device model is designated as *Case CIS-Ref* and is used as the reference case to compare the influence of traps or recombination centers on the device performance.

The J-V curve for this ideal case is shown in Figure 1-4 for both dark and illuminated conditions. The efficiency of the reference cell, η = 14.36%, is reasonable when compared to the experimental values for a pure CIS cell of 12% ~ 14%. The CIS cell with a record efficiency, fabricated by researchers at the National Renewable Energy Laboratory [1-4], showed the following device performance parameters: V_{OC} = 0.491 V, J_{SC} = 41.1 mA/cm^2, F.F. = 0.719, and η = 19.5%. Compared to the performance parameters of the record CIS cell, the simulation results for the reference case CIS-Ref shows higher V_{OC} and F.F. values, which can be explained by the absence of trap states and of a finite series resistance in the simulation. The lower value of J_{SC} for the CIS-Ref model can be attributed to the higher level of doping in the CIS layer than that of the record cell.

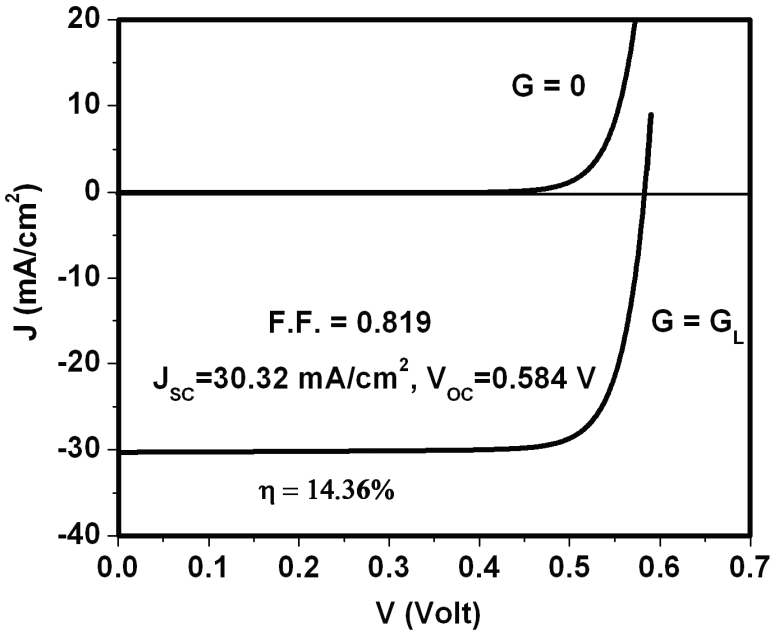

Figure 1-4. Simulated dark and AM0 J-V curves of the reference cell. Case: CIS-Ref.

1.3.2 Impact of Deeper Acceptors and Compensating Donors in the CIS Layer

The influence of compensating donors in a pure CIS cell was studied for the 3 cases summarized in Table 1-2. In the first case (CIS2) the acceptor level was increased from 80 to 240 meV. This increase in energy level will change the equivalent thermally activated hole concentration. In each calculation, the hole and electron lifetimes were kept equal at a value of 10^{-6} s. The effect of the deeper acceptor state, or of the compensating donors in the absorber, on the J-V characteristics is shown in the Figure 1-5. The corresponding values of V_{OC}, J_{SC}, J_0, η and Fill Factor, F.F. are shown in Table 1-3.

Table 1-2. Properties of each cell for the study of the compensation effect.

Cell	Comments
CIS-Ref	Reference cell (only acceptor states in CIS, E_A = 80 meV, $N_A = 8\times10^{16}$ cm^{-3})
CIS2	Deeper acceptor level (E_A = 240 meV)
CIS3	Compensation donor states (E_D = 240 meV, $N_D = 8\times10^{16}$ cm^{-3}, $\tau_p=\tau_n=10^{-6}$ s)
CIS4	Complete compensation by donor states (E_D = 80 meV, $N_D = 8\times10^{16}$ cm^{-3})

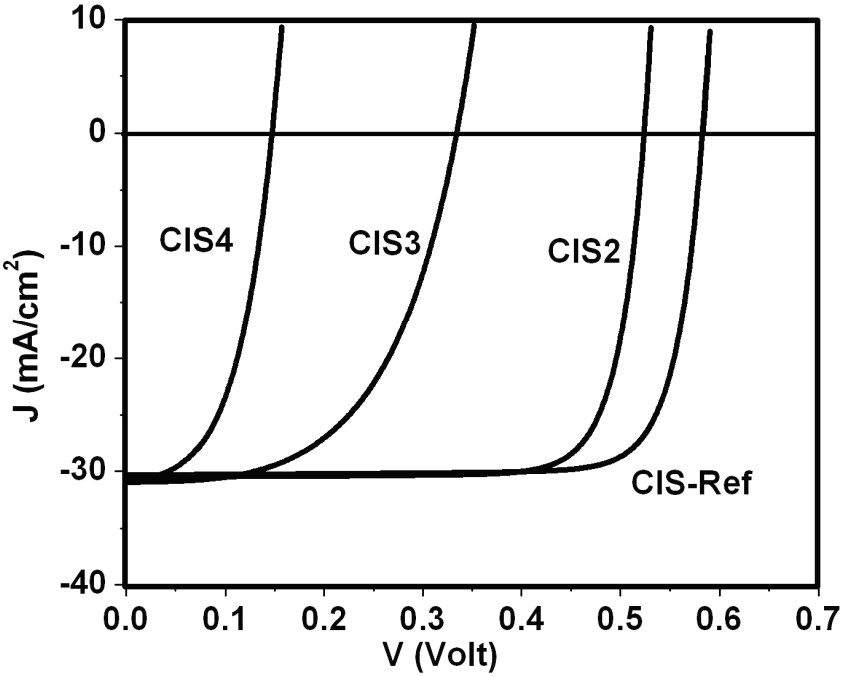

Figure 1-5. Compensation effect by donor states in the absorber layer.

Table 1-3. Performances for different acceptor level and for compensating donors.

	J_{SC}(mA/cm^2)	V_{OC} (V)	J_0 (mA/cm^2)	F.F	η(%)
CIS1	30.32	0.584	$\leq 10^{-10}$	0.81	14.36
CIS2	30.49	0.524	4.92×10^{-8}	0.80	12.81
CIS3	30.96	0.335	3.14×10^{-2}	0.54	5.65
CIS4	30.96	0.148	3.66×10^{-1}	0.51	2.34

Table 1-3 reveals that , as expected, each change decreased the value of V_{OC}, while there is almost no change in J_{SC}. The value of the V_{OC} is related to the dark saturation current, and physically, the maximum V_{OC} is limited by the built-in potential across the p-n junction. The potential is determined by the Fermi level of the n-CdS and p-CIS layers. Thus, it is reasonable that V_{OC} decreases for a deeper acceptor state since the hole concentration decreases.

1.3.3 Impact of Electrons, Hole Traps, and Recombination Centers in the CIS Layer

The effects of the trap states as well as recombination centers on the device performance are also studied for the cells given in Table 1-4. The energy levels are located at 200 meV above midgap for electron traps and at 200 meV below midgap for hole traps. Also, the lifetime of the carriers are calculated using reasonable values for the carrier capture cross sections, namely σ_p =

$\sigma_n = 10^{-15}$ cm^2, along with and the equation

$$\tau_{n,p} = \frac{1}{\sigma_{n,p} \nu_T^{n,p} N_T}, \quad \nu_T^{n,p} = (8kT/\pi m^*)^{1/2}, m_n^* = 0.2m_0, m_p^* = 0.8m_0,$$
$$m_0 = 9.11 \times 10^{-31} kg \tag{1-16}$$

where $\tau_{n,p}$ is the carrier lifetime at trap states, $\nu_T^{n,p}$ is the thermal velocity of carriers, N_T is the density of trap states, $m^*_{n,p}$ is the effective mass of the electron or hole. The capture cross-section adopted is an intermediate value based on the reported ranges of $\sigma = 10^{-16} \sim 10^{-14}$ cm^{-2}, experimentally measured for silicon bicrystals [1-5, 1-6]

The resulting current-voltage characteristics of the cells with traps and recombination centers are shown in Figure 1-6. As shown in the figure, only the short circuit current decreased in the case of CIS5, since electron traps reduce the electron concentration and the electron is the minority carrier and contributes to the short circuit current.

Table 1-4. Properties of each cell for the study of the effect of traps.

Cell	Comments
CIS-Ref	Reference cell (only acceptor states in CIS, E_A = 80 meV, $N_A = 8\times10^{16}$ cm^{-3})
CIS5	Electron traps (E_t = 320 meV below CB, $N_t = 5\times10^{19}$ cm^{-3}, $\tau_p=\tau_n=10^{-6}$ s)
CIS6	Hole traps (E_t = 320 meV above VB, $N_t = 1\times10^{18}$ cm^{-3}, $\tau_p=\tau_n=10^{-6}$ s)
CIS7	Recombination center ($E_t = E_i$, $N_t = 1\times10^{17}$ cm^{-3}, $\tau_p = 8.2\times10^{-10}$ s, $\tau_n = 4.1\times10^{-10}$ s)

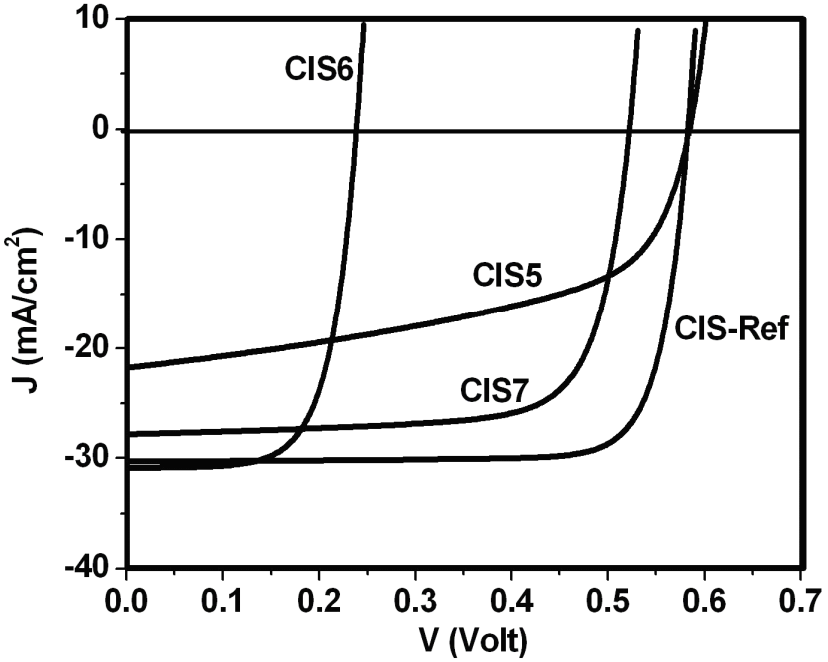

Figure 1-6. Effect of traps in the absorber layer.

In contrast, for simulation CIS6, only the open circuit voltage decreased as hole traps decreased the majority carriers and the Fermi level of absorber layer, which results in decreased built-in potential. When there are recombination centers, the concentrations of both electrons and holes decrease due to the SRH recombination. Therefore, both J_{SC} and V_{OC} decrease as in simulation CIS7 in Figure 1-6. The performance parameters for each cell are summarized in Table 1-5.

Table 1-5. Performance of each solar cell for the study of the effect of traps.

Cell	J_{SC}(mA/cm^2)	V_{OC} (V)	J_0 (mA/cm^2)	F.F	η(%)
CIS-Ref	30.32	0.584	$\leq 10^{-10}$	0.81	14.36
CIS5	21.79	0.584	$\leq 10^{-10}$	0.53	6.80
CIS6	30.90	0.239	1.28×10^{-4}	0.67	4.96
CIS7	27.86	0.523	6.06×10^{-4}	0.74	10.77

1.3.4 Impact of Grain Boundaries

Considering trap states at the grain boundary of p-type material as in Figure 1-7, initially, most of the trap states will be unoccupied as the Fermi level is below most of the trap levels. Therefore, most trap states are filled with holes and there is a positive charge build-up. The

positive charge build-up, in turn, results in the formation of a depletion region with higher electron density than the hole density near the grain boundary. Also, electrons are attracted to the trap states filled with holes, and they fill the trap states by recombining with holes. This increase of the occupancy of the trap states by electrons lowers the net positive charge initially formed at the grain boundary. Therefore, the positive charge or the potential formed at the grain boundary will find their equilibrium values depending on the doping level, light injection, and trap density. At thermal equilibrium, the Fermi level is located near the midgap, as in the case of the intrinsic semiconductor depicted in Figure 1-7.

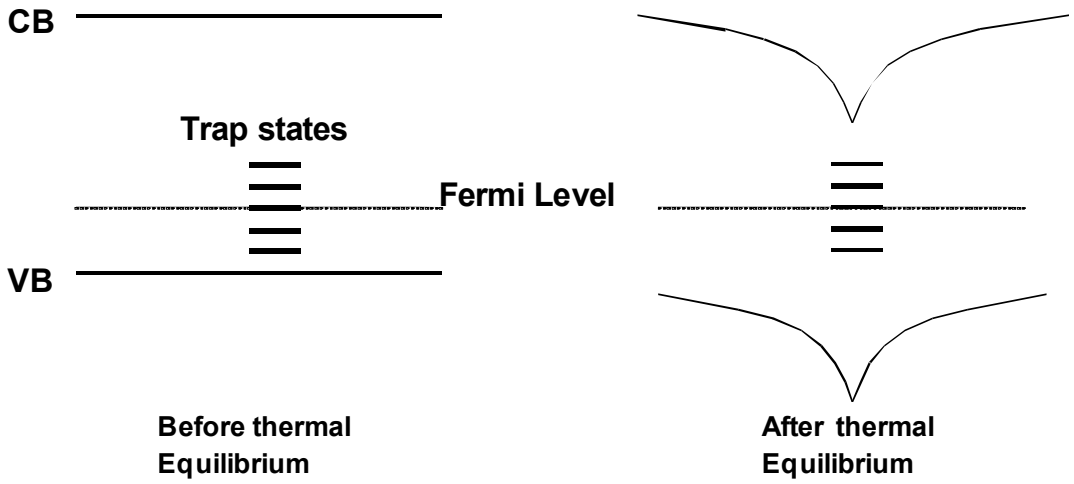

Figure 1-7. Energy band diagrams near a grain boundary region in the p-type material with trap states before and after equilibrium is obtained.

It is instructive to consider the impact of grain boundaries in a one-dimensional simulation before moving to the two-dimensional simulation. For the one-dimensional simulation it is assumed that a grain boundary exists at the center position of the CIS layer, which lies horizontally in the middle of the CIS layer. The localized trap state density was 3×10^{11}cm^{-2} and the carrier lifetimes are $\tau_p = \tau_n = 1\times10^{-9}$ s at the midgap position ($E_t = E_i$). The recombination of carriers at these trap states as well as trapping of holes was assumed to occur by SRH recombination.

The calculated current-voltage characteristics are shown in Figure 1-8. It is observed that both J_{SC} and V_{OC} decreased compared to the values of the reference case shown in Figure 1-4 without grain boundaries. This is due to a decrease in the hole density produced by the trap states, as well as the recombination of electrons with holes at the trap states that occurs to reach equilibrium as described in the explanation found in the caption of Figure 1-7. Energy-band diagrams are shown in Figures 1-9 and 1-10 for the simulations that include light and those without light, respectively, when no bias ($V_{applied} = 0$) is applied. Band bending due to the grain boundary trap states is observed in Figure 1-9. From the observed band bending it is suggested that there is a positive charge that has accumulated at the grain boundary, and the grain boundary potential was found to be 0.358 eV.

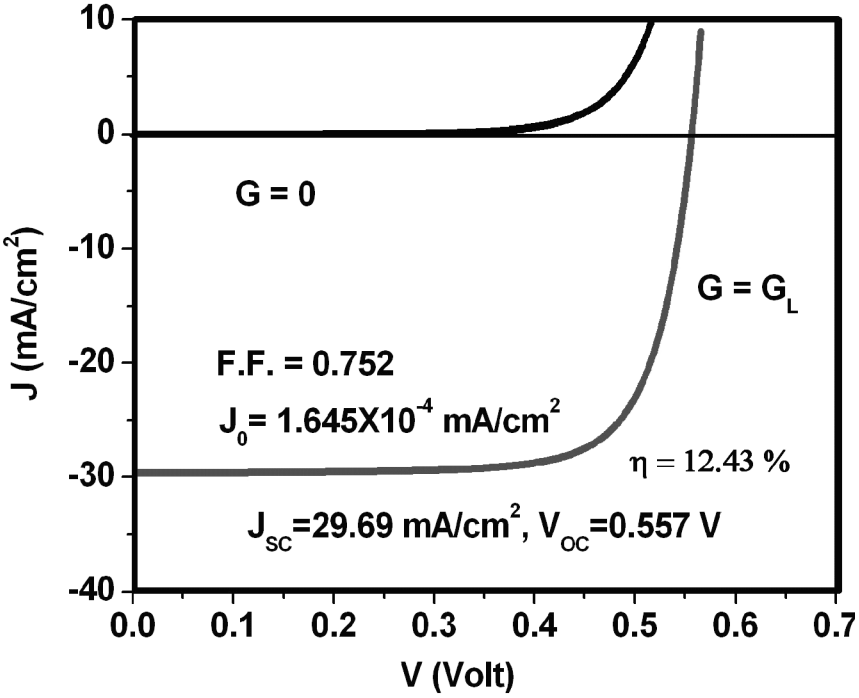

Figure 1-8. Current-voltage characteristics of a solar cell with a grain boundary at the center of the absorber layer.

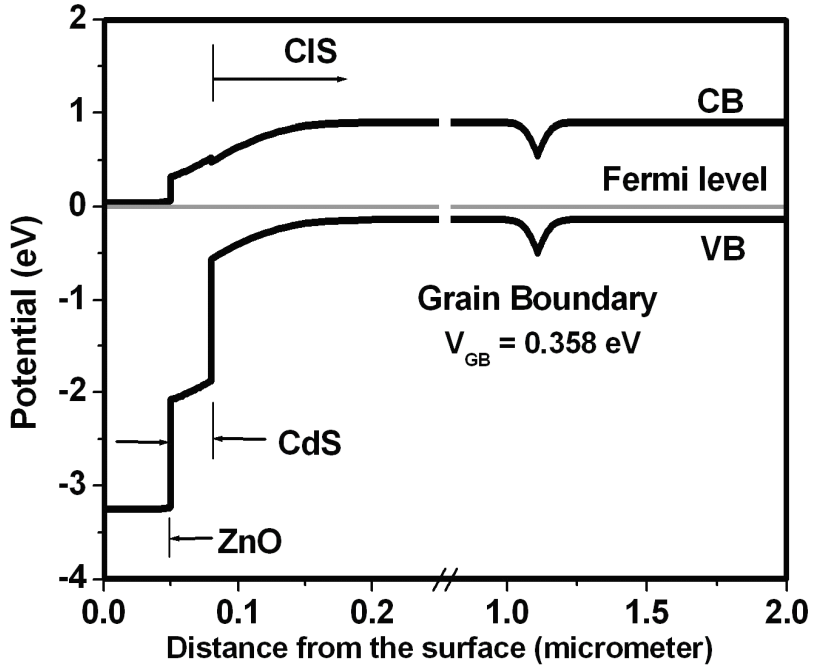

Figure 1-9. Band diagram of the solar cell with a grain boundary at the center of the absorber layer with no illumination.

Figure 1-10 shows the band diagram for the case with illumination and it is observed that the grain boundary potential decreased from its value for the dark condition. Also, the minority carrier current, electrons in the CIS layer, flows in the direction normal to the grain boundary as it is the direction where the potential gradient has its largest value.

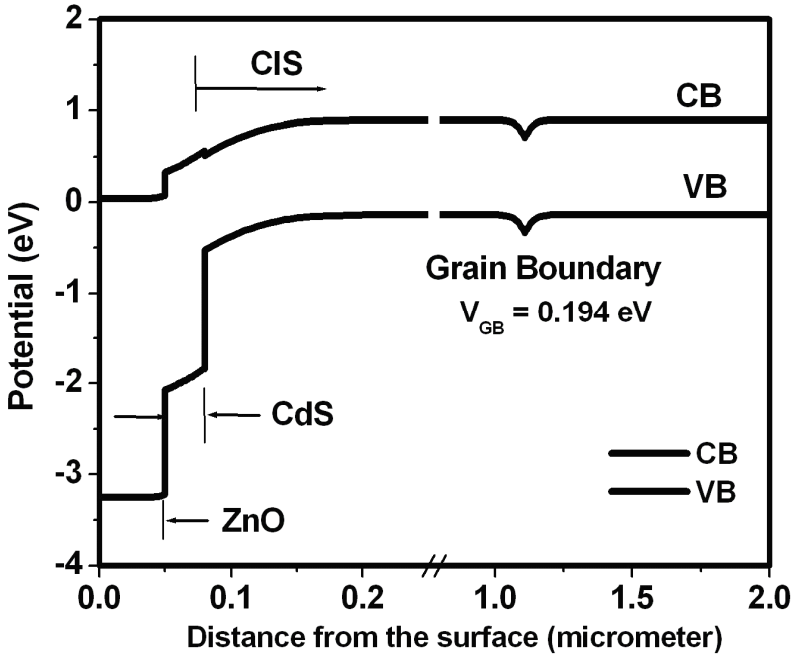

Figure 1-10. Band diagram of the solar cell with a grain boundary at the center of the absorber layer with illumination.

1.4 Two-Dimensional Simulation Study

1.4.1 Grain-Boundary Effect for a Square Rectangular Grain

The problem of a cell with rectangular grain boundaries is three-dimensional since the cell structure consists of different layers in the z-direction, and the grain boundaries produce variations normal to their surfaces. The simple case of two horizontally aligned grains is the one-dimensional problem addressed in Section 1.3.3. That case, however, does not reflect the observed grain structures found in CIS cells. If we consider the grain boundaries as rectangular grains, as shown schematically in Figure 1-11a, the problem should be solved in three-dimensions, or with periodic boundary conditions on the outside boundary of the domain. It is possible to construct a two-dimensional problem assuming a right cylindrical geometry of the grain (see Figure 1-11b). Also, if we try to solve the problem using axisymmetry conditions, the actual grains considered in the problem become annular grains (Figure 1-11b).

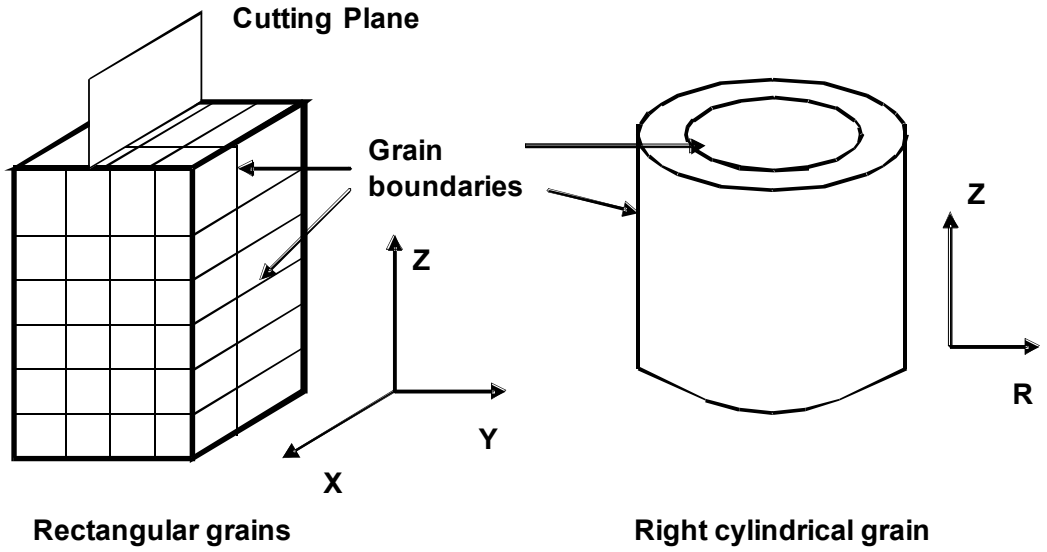

(a) (b)

Figure 1-11. Consideration of grain boundaries in three-dimensional space.

In this research, the effect of grain boundaries is simulated using the domain formed upon slicing the structure parallel to the z-axis with a plane bisecting two grain boundaries. Therefore, the structure solved has grain boundaries that are parallel to X-Z and X-Y planes. The grain of square rectangular type explored in this research requires specifying a characteristic length. The characteristic number is the surface-area-to-volume ratio of the grains. Figure 1-12 shows a schematic of the actual domain solved in this study. In this problem, the boundary condition imposed at the symmetry plane was of the Neumann type, which requires that n•**Del** V = 0. This condition is equivalent to requiring no surface charge on this symmetry plane, and it also requires that the current not flow across this plane and that the normal component of the electric field is zero.

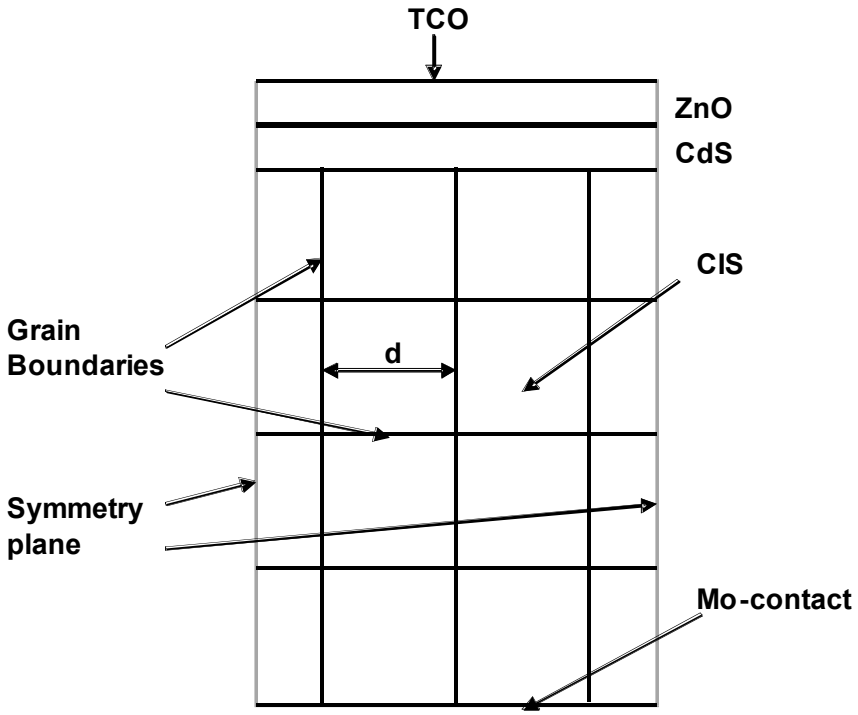

Figure 1-12. Simplification of grain boundaries solved in this study.

Grain boundaries can influence device performance if they contain traps at the interfaces. This influence can be considered by evaluating the effects of the carrier lifetime at the trap state, as well as the number density of the trap states and its energy level. Because there are traps at the grain boundaries, the lifetimes of the carrier at the grain boundaries decrease compared to their bulk lifetime values. The effective lifetime is determined by the lifetime at the grain boundaries, τ_g. The lifetime associated with the trap states is defined as

$$\tau_g = \frac{1}{\sigma_g v_{th} N_t} \quad or \quad \frac{1}{\tau_g} = \sigma_g v_{th} N_t \tag{1-17}$$

where σ_g is the capture cross section of the trap state, ν_{th} is the thermal velocity of carrier, and N_t is the number density of trap states. For cubic and spherical grains, the effective density of trap states in the bulk, N_t (cm^{-3}), for a given trap density at the grain boundaries, N_{ts}, can be defined by the following conservation equation:

$$SN_{ts} = N_t V, \quad 6d^2 N_{ts} = N_t d^3 (cubic) \quad or \quad \pi d^2 N_{ts} = \frac{\pi}{6} d^3 N_t (spherical), \tag{1-18}$$

where S is the surface area of a grain and V is the volume of a grain. Thus, the effective density of trap states in the bulk is defined as $N_t = 6N_{ts}/d$. The effective grain size is defined as the ratio of the volume of the grain to the surface area multiplied by 6, as $d_{eff} = 6V/S$, $d_{eff} = d$ for the case with cubic grains. In this case, from Equation (1-17) and (1-18), the following relations are

obtained:

$$\tau_g = \frac{1}{\sigma_g v_{th} N_t} = \frac{d_{eff}}{\sigma_g v_{th} N_{ts}} \quad defining \quad \sigma_g v_{th} N_0 = \frac{1}{\tau_{g0}}, \quad where \quad N_0 = 10^{16}\, cm^{-3},$$
$$\frac{1}{\tau_{go}} \sim 10^7\, s \quad then \quad \frac{\tau_{g0}}{\tau_g} = \frac{1}{d_{eff}} \frac{N_{ts}}{N_0} \tag{1-19}$$

where τ_{g0} is calculated from the values of $\sigma_g = 10^{-14}$ cm^2 and $\nu_{th} = 10^7$ cm/s. Therefore, the effect of grain size is also considered in the carrier lifetime through Equation (1-19).

In the following two-dimensional simulations as well as the previous one-dimensional simulations, the grain boundary effect is studied by solving the continuity and Poisson equations self-consistently with trap states at the grain boundaries and the effective lifetime given by Equation (1-19), instead of just specifying the recombination velocity at the grain boundaries. Therefore, the grain boundary potential as well as the carrier concentration or Fermi level was determined self-consistently.

Solar cells with square rectangular grains of 0.2 μm size (distance between the grain boundary planes), were first studied to understand the effect of grain boundaries on the electrical properties of the cell. Figure 1-13 shows the J-V characteristics of cells with and without grain boundaries.

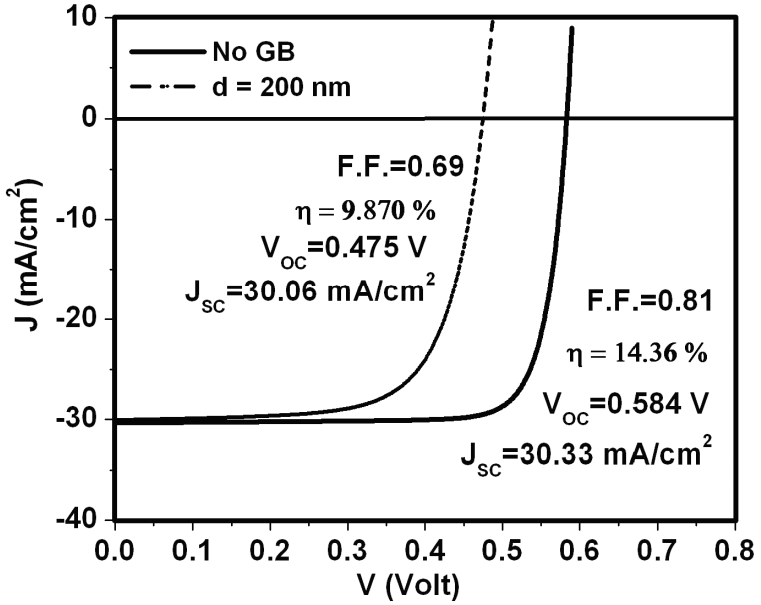

Figure 1-13. Comparison of J-V characteristics for the case with (d = 200 nm) and without grain boundaries.

As shown in Figure 1-13, the trap states mainly act as the hole traps as the midgap traps are

filled with holes from the adjacent p-type absorber layer. Also, a small decrease of J_{SC} is calculated, which is due to the recombination of electrons with the holes trapped at the grain boundary states. At the equilibrium state (i.e., no light injection), positive charge is accumulated at the grain boundaries by the trapping of holes. Upon illuminating, the positively charged grain boundaries repel holes and attract electrons to the grain boundaries. Therefore, there are few holes available in the grain boundary depletion region to recombine with electrons.

The current flow lines for the solar cells with 200 nm spaced grain boundaries are shown in Figure 1-14.

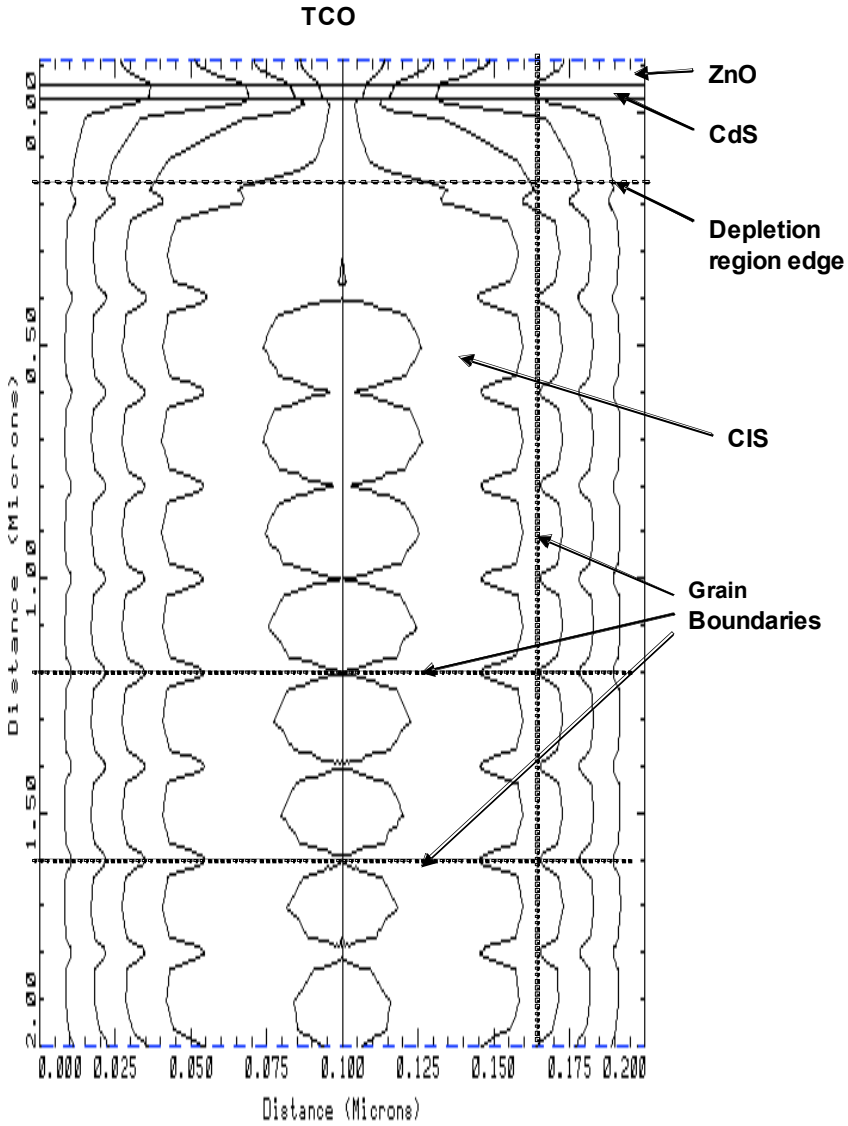

Figure 1-14. Current flow line of the solar cell with grain boundaries (d = 200 nm), the length in width direction in this figure is exaggerated.

In Figure 1-14 the current flow lines cross the grain boundary planes at 90°, which was previously reported [1-7]. The corresponding net carrier density and the potential surface are

shown in the Figures 1-15 and 1-16. The depletion of carriers and potential increase along the grain boundaries are apparent in this result. The effect is strongest where the grain boundaries intersect.

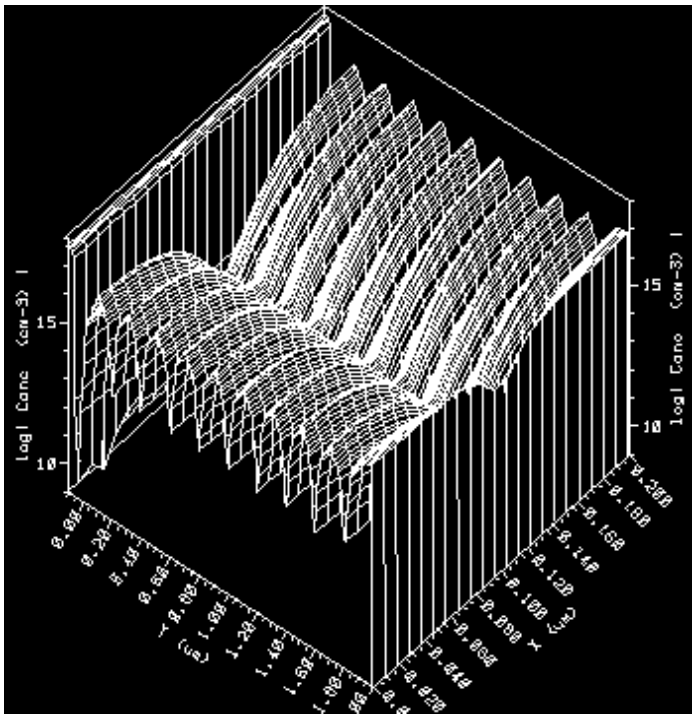

Figure 1-15. Surface plot of the net carrier density (d= 200nm).

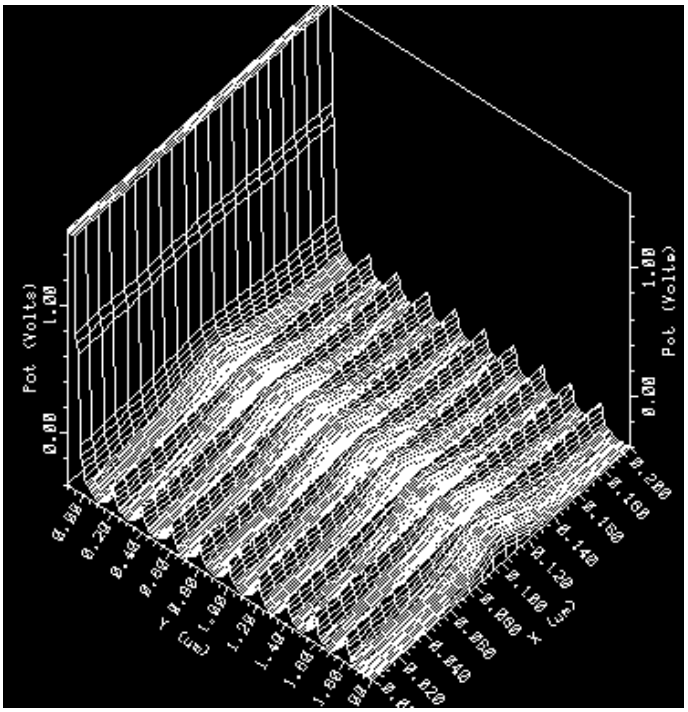

Figure 1-16. Surface plot of the potential for the cell with grain boundaries (d = 200 nm).

It is important to investigate the effect of grain boundaries as a function of grain size, as grain size control has been greatly studied by the community. Therefore, in this research work the effect of grain size was studied by changing the grain size, which resulted in the change of equivalent trap density, N_t, and the carrier lifetime as in Equations 1-18 and 1-19. The simulations were performed and the resulting device performance characteristics J_{SC}, V_{OC}, F.F., η and dark saturation current, J_0, as well as the grain boundary potential are plotted as a function of effective grain size as in Figures 1-17 through 1-21. The effective grain size is the rectangular grain size equivalent to that of spherical grains. For example, in the case of the square rectangular grain, the volume to the grain boundary surface area ratio of the grain is $d^2L/(4dL) = d/4$, where L is the length of the rectangle, which is 1.5 times the effective grain size, $d_{eff} = d/6$, as in the case of spherical grains.

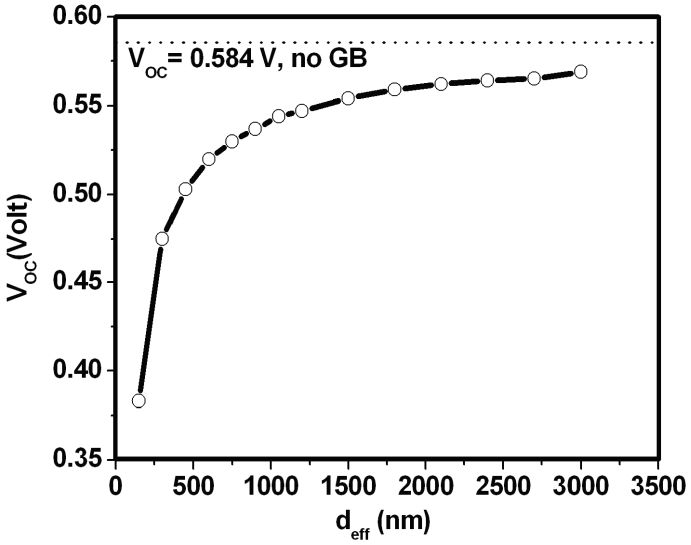

Figure 1-17. Voc of solar cells as a function of effective grain size.

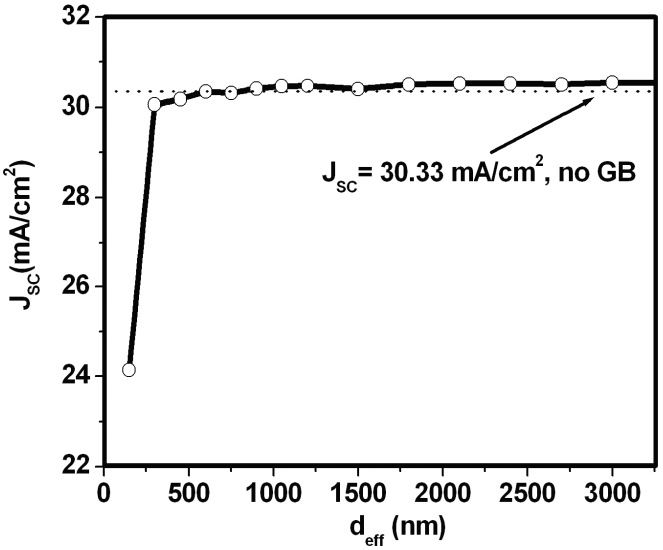

Figure 1-18. J_{SC} of solar cells as a function of effective grain size.

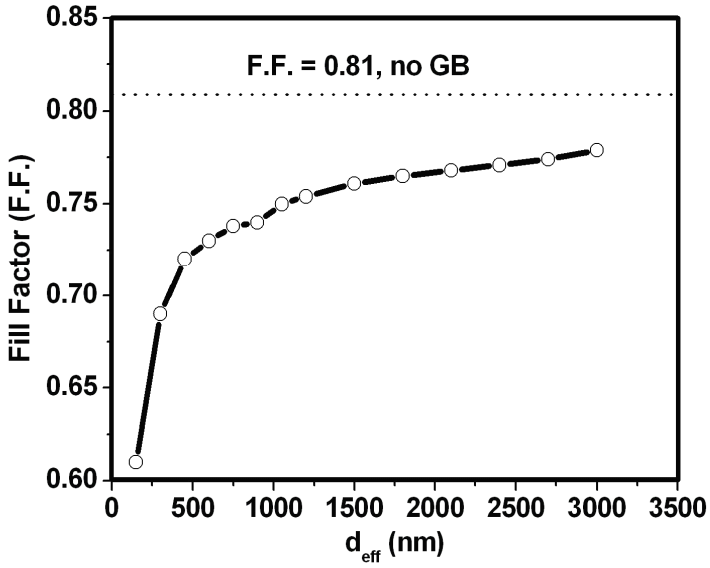

Figure 1-19. Fill factor of solar cells as a function of effective grain size.

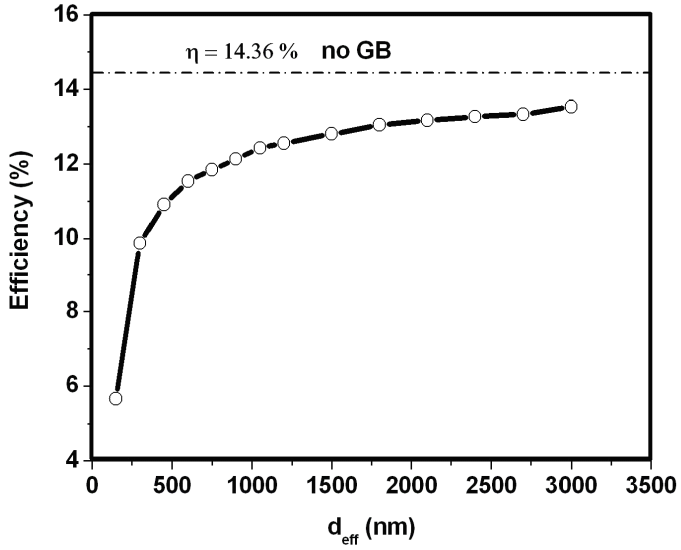

Figure 1-20. Efficiency of solar cells as a function of effective grain size.

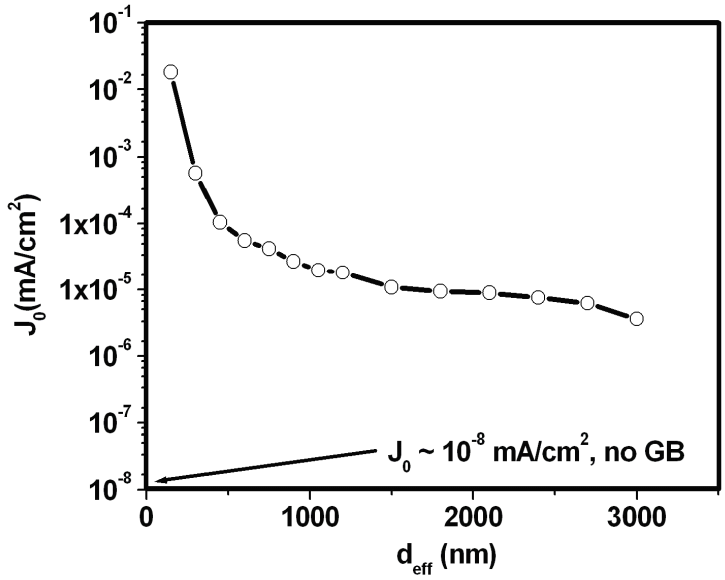

Figure 1-21. J_0 of solar cells as a function of effective grain size.

Therefore, the grain size (precisely, the distance between the grain boundaries in this case) was recalibrated by multiplying the original value by 1.5. From the figures, it is observed that V_{OC} decreases by the trapping of holes at the grain boundary states, which resulted in a decrease of efficiency. On the other hand, J_{SC} remains unchanged until the grain size becomes smaller than 0.3 μm. It is suggested that this grain size is related to the length of the grain boundary depletion region as $d_{critical} \sim 2L_{depletion\ region}$. The dark saturation current, J_0 is found to increase as the grain size decreases. It is suggested in [1-8] that the reverse saturation current J_0 is composed of the diffusion current term and the recombination current term. They assumed that the recombination current term dominates J_0 for the small grains and suggested the relation of $J_0 \sim d^{-1}$, and this relationship showed agreement with experimental data. The experimental data, however, was limited. The results of our simulation did not follow this relation. Figure 1-22 is a plot of J_0 as a function of grain size in a log scale.

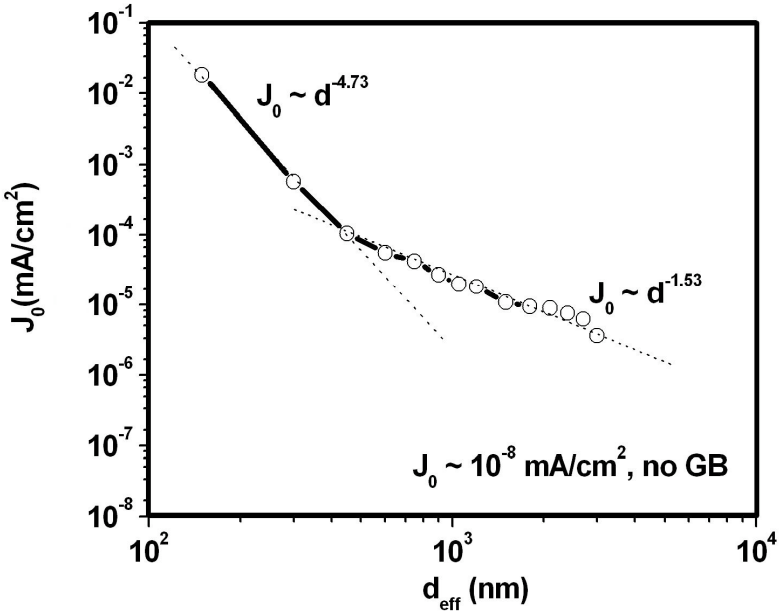

Figure 1-22. J_0 of solar cells as a function of effective grain size in log scale.

As clearly shown in Figure 1-22, there are two regions with different dependence of J_0 on the effective grain size. For $d_{eff} > 450$ nm, J_0 shows the dependence on $d^{-1.53}$. For this case, it is proposed that the width of grain boundary depletion region is smaller than the half of the effective grain size, which means the depletion of the grain interior is incomplete in this case. If this is the case, there should be a diffusion of electrons to the edge of grain boundary depletion region to be swept by the electric field and to recombine with holes at grain boundary trap states. For this situation, the diffusion process may be the rate-determining step. Upon considering the expression of the dark saturation current by diffusion, the following scaling relation can be obtained:

$$J_0 \approx J_0^{diffusion} \approx 1/L_n p \sim d^{-0.5} d^{-1} \sim d^{-1.5}$$
$$, where \quad L_n = (D_n \tau_n)^{1/2} \quad , \quad \tau_n \approx \tau_g \sim d \quad and \quad p \sim N_t^{-1} \sim d \tag{1-20}$$

where L_n is the diffusion length of electrons in CIS layer, p is the hole density in CIS layer, D_n is the diffusion constant for electrons in CIS layer, τ_n is the electron lifetime in CIS layer, which is determined by the smallest value, τ_g, and N_t is the equivalent density of grain boundary trap states in the bulk of CIS layer. The scaling relation between J_0 and d, $J_0 \sim d^{-1.5}$, obtained shows good agreement with the exponent of d form the results by simulation.

When the effective grain size is smaller than 450 nm, the grain size can be smaller than $2L_{GB\ depletion\ region}$, which results in the total depletion of the grain interior and the electrons will be instantly swept by the electric field and recombine with the holes. In this case, the dark saturation current is determined by the recombination current term and can be represented in Equation (1-21) as in [1-9].

$$J_0 \approx J_0^{recmbination} \approx 2qS_n(W)n(W), \quad where \quad S_n(W) = \frac{1}{2}v\sigma N_{ts} \exp(qV_{GB}/kT) \tag{1-21}$$

where q is a charge of electron, $S_n(W)$ is the recombination velocity at the edge of grain boundary depletion region, n(W) is the electron density at the edge of grain boundary depletion region, ν is the velocity of electrons that is not necessarily the same as the thermal velocity, σ is the capture cross section of electrons at grain boundary trap states, and V_{GB} is the grain boundary potential.

Upon considering Equation (1-21), it can be suggested that only ν and V_{GB} are strong functions of the grain size. Therefore, it is suggested that the exponent of $d^{-4.73}$ comes from the dependence of the term, $\nu\exp(qV_{GB}/kT)$, on the grain size. To find the value for the width of the grain boundary depletion region, the net carrier density is plotted from top surface of the cell along the depth as in Figures 1-23 and 1-24. From the result for the case without illumination, the critical effective grain size, where d_{eff} is equal to the twice the width of the grain boundary depletion region, $2L_{GB\ depletion\ region}$,was found to be between 300 nm and 450 nm. This value is close to the effective grain size, d_{eff} = 450 nm, where the dependence of J_0 on d_{eff} changes. Therefore, the previous assumption that the change of J_0 dependence on d_{eff} can be explained by the change of carrier transport mechanism for the recombination process reasonable. The critical effective grain size decreases to the value of 300 nm with illumination as shown in Figure 1-24, since the grain boundary potential and the resulting depletion region decreases with illumination from the supply of excess carriers by photogeneration.

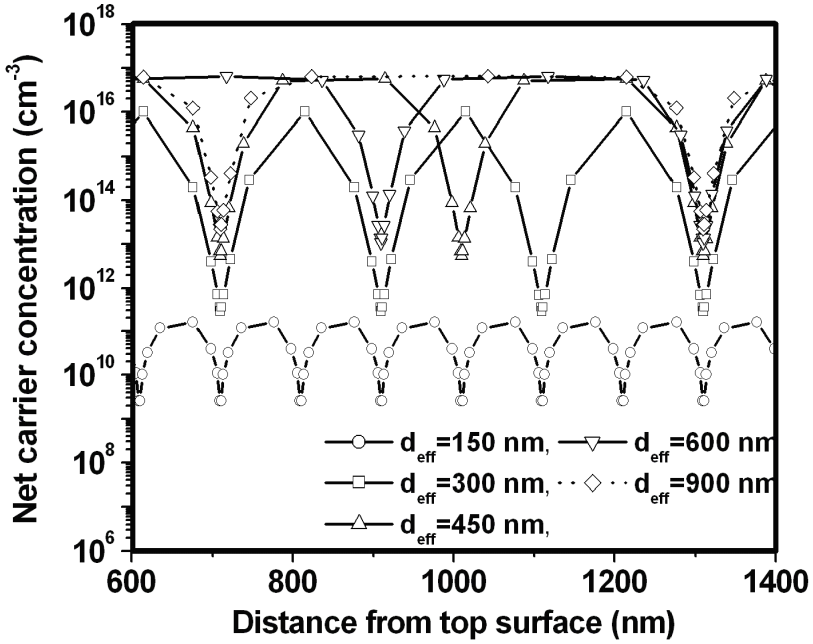

Figure 1-23. Net carrier distribution along the depth of the cell without illumination.

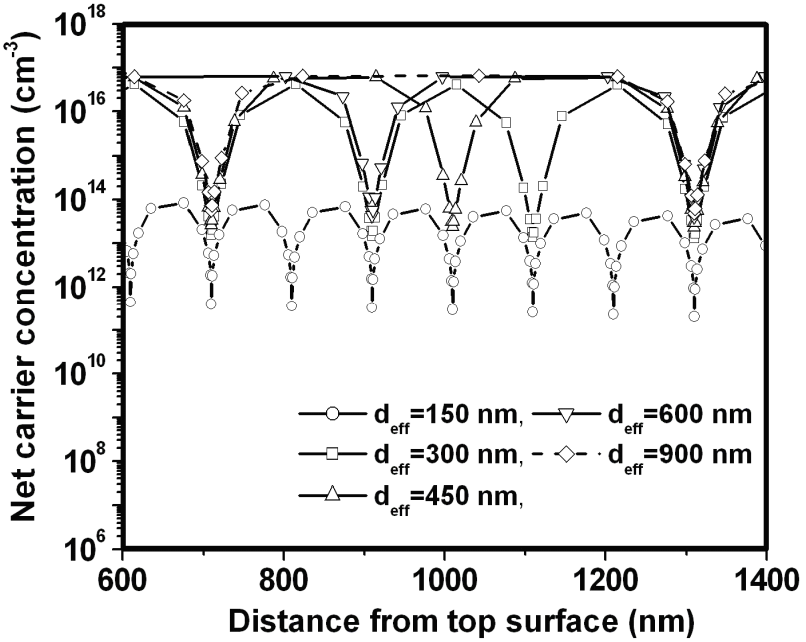

Figure 1-24. Net carrier distribution along the depth of the cell with illumination.

The potential along the depth of the solar cell at the center of the grain is plotted in Figures 1-25 and 1-26. It is observed that the grain boundary potential decreased almost by 100 meV with light injection for the case with 300 nm grains, while there is very slight decrease in the case of large grain size (d = 1200 nm).

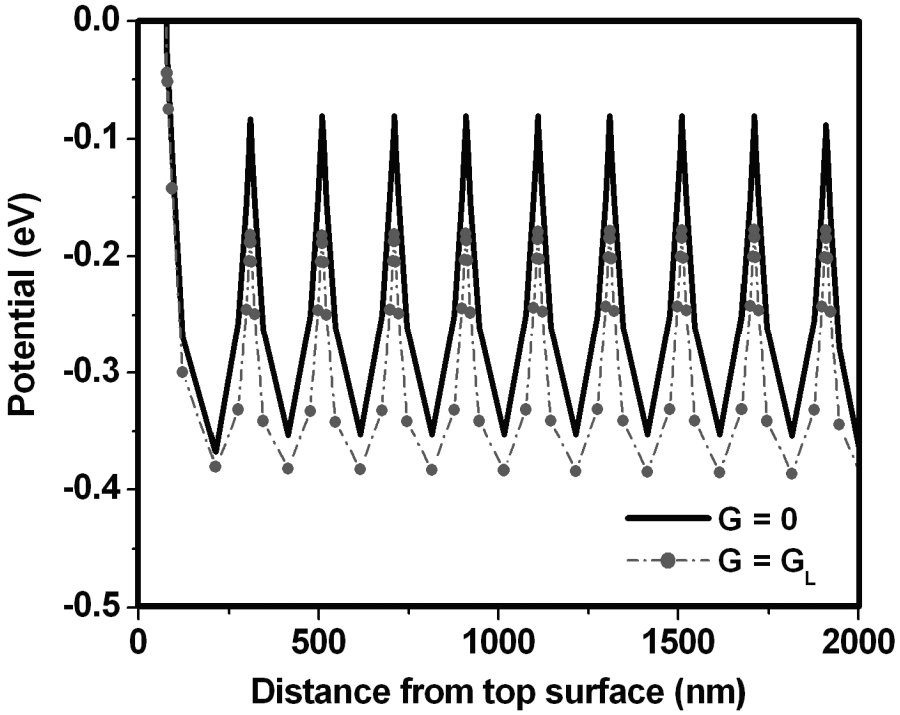

Figure 1-25. Potential along the depth of the solar cells ($N_T = 10^{12}$ cm^{-2}, $d_{eff} = 300$ nm).

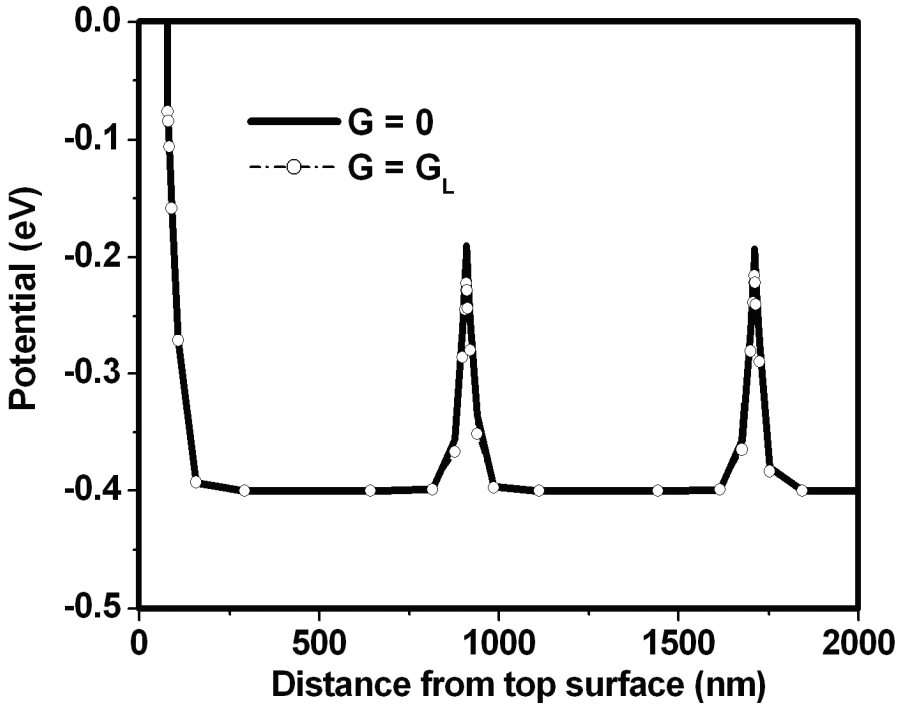

Figure 1-26. Potential along the depth of the solar cells ($N_T = 10^{12}$ cm^{-2}, $d_{eff} = 1200$ nm).

This difference is a result of the grain being nearly fully depleted at small grain sizes because the impact of adjacent grains overlap. Thus, the supply of holes as well as electrons with illumination decreases the charge accumulation at the grain boundaries and produces a new steady-state charge distribution. It is also observed in the figure that the grain boundary potential increases with decreasing grain size. When the grain size decreases, the probability of filling the trap states with holes increases as the equivalent trap density in the bulk CIS layer, N_t, increases. Therefore, there is more positive charge build-up and the increase of grain boundary potential at grain boundaries.

Figure 1-27 shows the effect of the trap density at the grain boundaries on the potential profile of the solar cell.

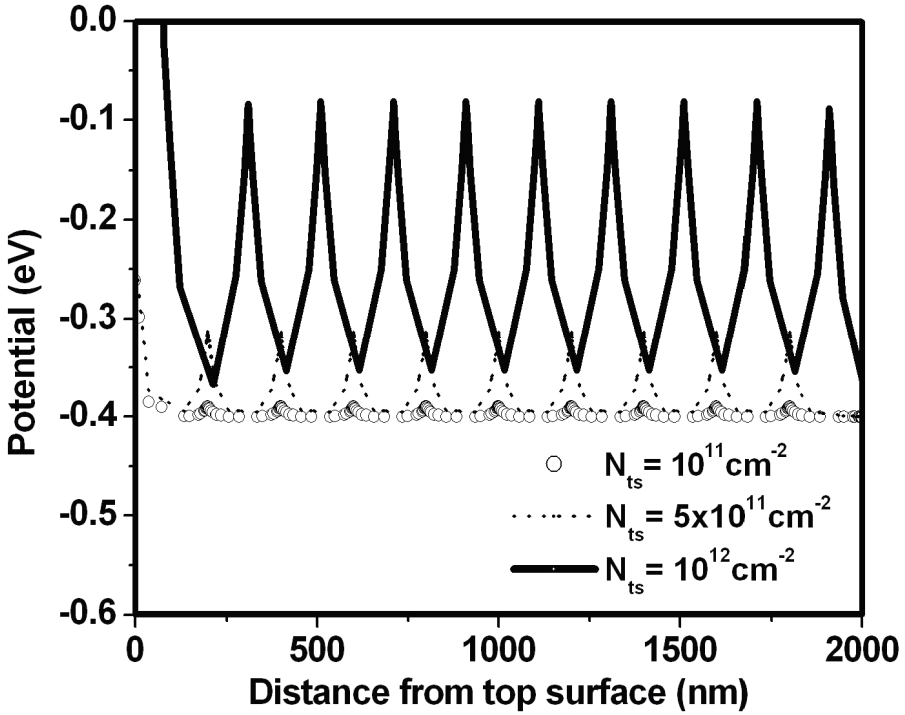

Figure 1-27. Potential variation for different trap density along the grain boundaries (d = 200 nm).

The calculation shows that the grain boundary potential or the barrier height for hole transport decreases with decreasing trap density as the probability of filling the trap states with holes decreases with decreasing trap density.

1.4.2 Effect of the Grain-Boundary Orientation

In the real solar cells, the absorber layers of the best cells are known to have the columnar grain structures or vertically oriented grain boundaries. Also, it is required to have the minority carrier transport in the thickness direction of the absorber layer to obtain the solar cells with good performance. Therefore, it is expected that grain boundaries with different orientation affect the device performance in a different manner.

In this section, the orientation of grain boundaries were studied by considering the grain boundaries with only one orientation, which are vertical-only grain boundaries (VGB) and horizontal-only grain boundaries (HGB) as in Figure 1-28.

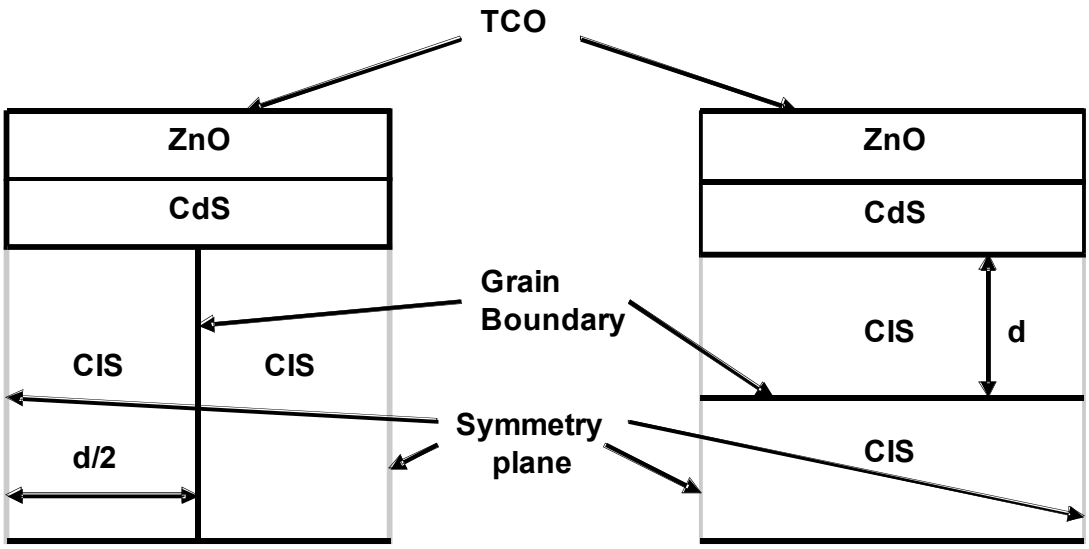

Figure 1-28. Schematic diagram of VGB and HGB solved in this study

As in Figure 1-28, the effective grain size in VGB and HGB are defined as the ratio of the volume of the grain to the grain boundary surfaces multiplied by 6 as before:

$$d_{eff} = 6V / S = 6dWL/(2WL) = 3d = 3d_{cubic} = 2d_{square\ \ rectangular} \tag{1-22}$$

Figures 1-29 through 1-33 are the device performance characteristics J_{SC}, V_{OC}, F.F., η, and dark saturation current, density J_0, (as well as the grain boundary potential) as a function of effective grain size. The results for the case with square rectangular grains are also included in the figures for the comparison purpose. Figure 1-29 shows that VGB shows more effect on V_{OC} than HGB and the value of V_{OC} when the grain size is large is also small for the case of VGB. From the calculation it was found that the length of the depletion region in the CIS layer is 88 nm, consistent with the previous discussion.

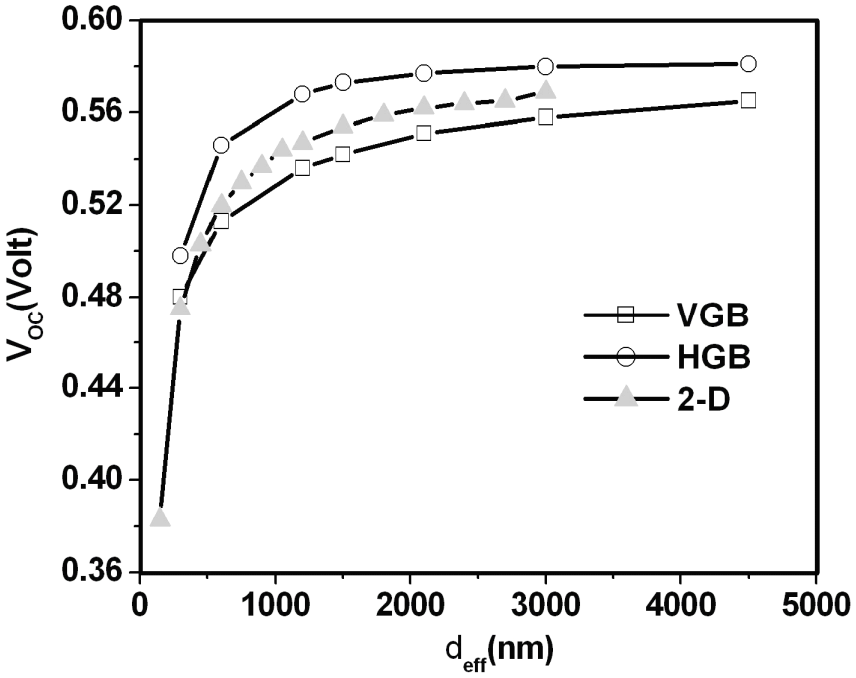

Figure 1-29. Effect of grain boundary orientation on V_{OC}.

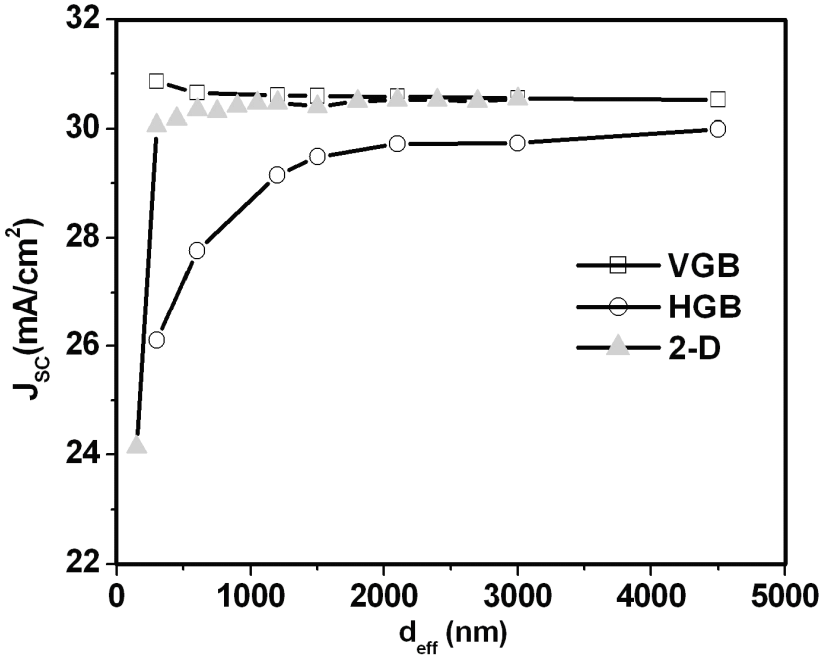

Figure 1-30. Effect of grain boundary orientation on J_{SC}.

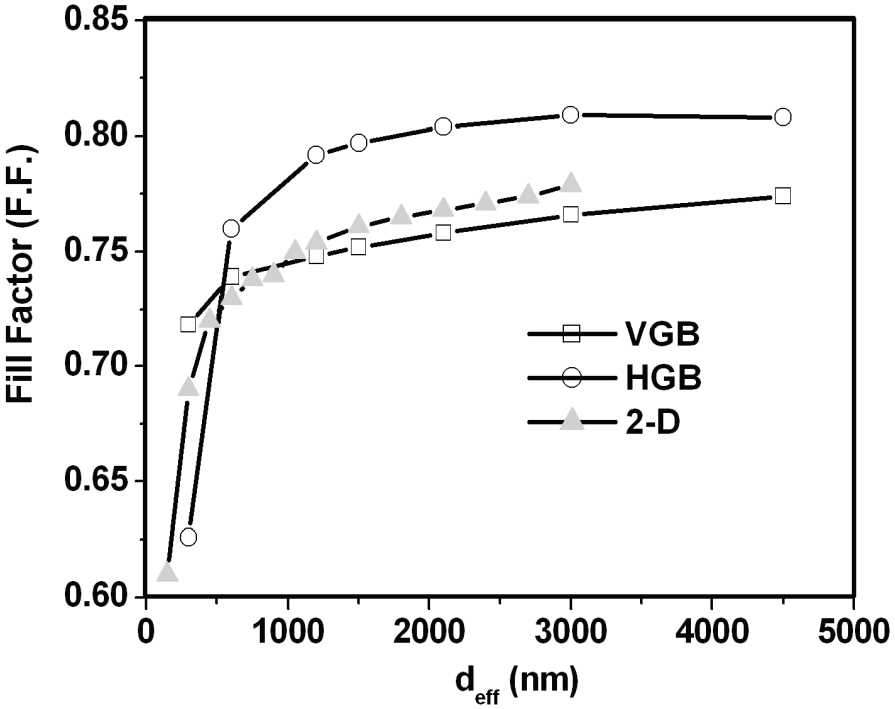

Figure 1-31. Effect of grain boundary orientation on Fill Factor.

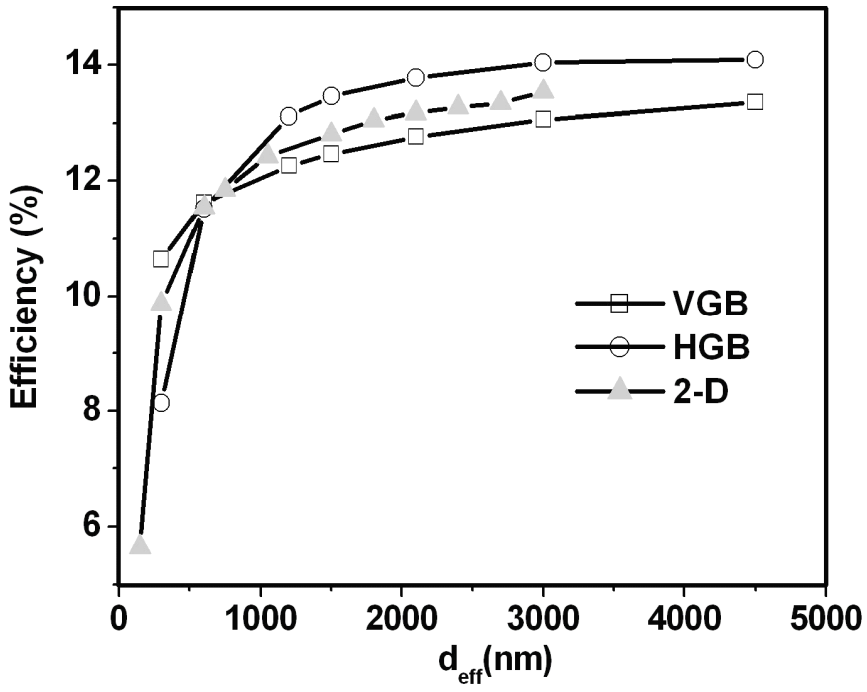

Figure 1-32. Effect of grain boundary orientation on efficiency.

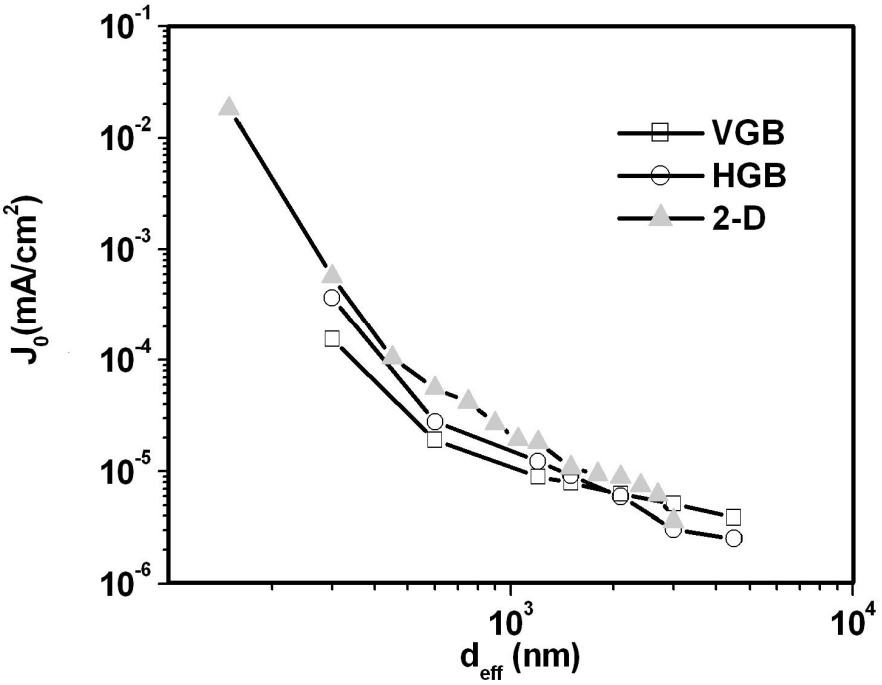

Figure 1-33. Effect of grain boundary orientation on J_0.

Therefore, even when d has the smallest value considered (d = 100 nm), there is no grain boundary in the junction depletion region in the case of HGB, while there are always grain boundaries in the case of the VGB regardless of the grain size. When the grain boundaries are in the junction depletion region, where the carriers are depleted, the effect of grain boundaries is enhanced by the increased recombination velocity due to the electric field, and the built-in potential that is related to V_{OC} decreases.

The short circuit current, J_{SC} shows different behavior from that of V_{OC} for the grain boundary orientation effect. While VGB remains almost constant with grain size, HGB shows lower value compared to the values in the case of VGB and decreases with grain size below the effective grain size of ~ 2000 nm. Contrary to the case of VGB, the minority carrier electrons should surmount the barrier at grain boundaries to reach the junction depletion region and to contribute J_{SC}. The decrease of J_{SC} in the case of HGB, therefore, can be attributed to the barrier effect of HGB that are normal to the transport of the electrons.

The efficiency as well as the fill factor show the combined behavior. When the grain size is large, VGB shows lower efficiency since the V_{OC} is lower in the case of VGB, while the differences in J_{SC} are not large. When the grain size is small, J_{SC} decreases rapidly in the case HGB and the differences of V_{OC} between VGB and HGB become negligible, which results in a lower efficiency for the case of HGB. The dark saturation current J_0 shows the similar behavior as the two-dimensional case with square rectangular grains.

1.4.3 Effect of the Junction Depletion Region on the Grain-Boundary Effect

As discussed in the section 1.3.4, the grain boundary potential at thermal equilibrium is

determined by the trapping of the holes at grain boundary states and the resulting recombination of the trapped holes with the electrons. As the carrier density and the transport process of the carriers are different for the quasi-neutral region and the junction depletion region, it is expected that the effect of grain boundaries should be different when the fraction of grain boundaries in the junction depletion region is different, or when the width of the junction depletion region changes.

In this section the effect of the junction depletion region on the grain boundary effect is studied by considering the effect of grain boundaries for the cases with VGB and HGB with higher CdS/CIS doping ratio of 15 (/6×10^{17} cm^{-3}/4×10^{16} cm^{-3}/) relative to the reference case with a ratio of 0.75 (/6×10^{16} cm^{-3}/8×10^{16} cm^{-3}/) doping ratio. This higher CdS/CIS doping ratio indicates an increase of the junction depletion region. From the solution of the Poisson equation, the length x_p of the depletion region in the p-side of the homojunction p-n diode, is given by

$$x_p = [\frac{2K_s\varepsilon_0}{q}\frac{N_D}{N_A(N_A+N_D)}V_{bi}]^{1/2} \quad , where \quad V_{bi} = \frac{kT}{q}\ln(\frac{N_A N_D}{n_i^2}) \tag{1-23}$$

and where K_s is the dielectric constant of the CIS layer, ε_0 is the dielectric constant of vacuum (8.85×10^{-14} F/cm), q is the charge of a electron, N_A is the doping of the p-type CIS layer, N_D is the doping of the n-type CdS layer, V_{bi} is the built-in potential of the p-n diode, n_i is the intrinsic carrier concentration for p-side and n-side, respectively.

From Equation (1-23) and the values of the parameter, x_p and V_{bi} for each case were calculated to obtain th results reported in Table 1-6. The doping density of the CIS layer for each case was calculated from the acceptor energy level of 80 meV from the valence band, and the density of acceptor state 8×10^{16} cm^{-3}, 4×10^{16} cm^{-3} for each doping ratio from the simulation.

Table 1-6. The length of the depletion region in the CIS layer and built-in potential in each doping ratio.

	Doping ratio (CdS/CIS)	V_{bi} (V)	x_p (nm)
Reference	(6×10^{16} cm^{-3}/6.6×10^{16} cm^{-3})	0.798	93
High doping ratio	(6×10^{17} cm^{-3}/3.6×10^{16} cm^{-3})	0.842	183

However, Equation (1-23) can be only applied for a homojunction diode. For the heterojunction p-n diode, Equation (1-23) can be modified to yield [1-10]

$$x_p = [\frac{2\varepsilon_{s,n}\varepsilon_{s,p}}{q}(\frac{N_D}{N_A(N_a\varepsilon_{s,p}+N_D\varepsilon_{s,n})})V_{bi}]^{1/2} \quad ,$$
$$where \quad V_{bi} = \frac{1}{q}[\frac{\Delta E_C - \Delta E_V}{2} + kT\ln(\frac{N_A N_D}{n_i^p n_i^n})] \tag{1-24}$$

and where $\varepsilon_{s,n}$ and $\varepsilon_{s,n}$ are the dielectric constant of CdS and CIS, K_s multiplied by ε_0 respectively, ΔE_C is the difference of the electron affinity, χ_p - χ_n, and ΔE_V is defined as χ_n - χ_p + E_g(CdS) - E_g(CIS). The values for each parameter are shown in Table 1-7, and values for V_{bi}

and x_p are given in Table 1-8.

Table 1-7. The parameters for the calculation of the depletion region in the CIS with heterojunctions equations.

	χ(eV)	E_g (eV)	n_i (cm^{-3})	$K_{S,}$	$N_{A,D}$ (cm^{-3})
CdS	3.75	2.4	1.28×10^{10}	13.6	6×10^{16}
CIS	3.8	1.04	0.04778	10.0	$6.6\times10^{16}/3.6\times10^{16}$

Table 1-8. The length of the depletion region in the CIS layer and built-in potential in each doping ratio with heterojunctions equations.

	Doping ratio (CdS/CIS)	V_{bi} (V)	x_p (nm)
Reference (HGB,VGB)	(6×10^{16} cm^{-3}/6.6×10^{16} cm^{-3})	0.850	88
High doping ratio (HGB_H, VGB_H)	(6×10^{17} cm^{-3}/3.6×10^{16} cm^{-3})	0.894	186

The values x_p obtained by Equation (1-24) in each case, are not much different from those resulting from Equation (1-23), and it is observed that the width of the p-side depletion region increased from 88 nm to 186 nm by increasing the doping ratio. The device performance parameters for the reference cases, HGB and VGB, and the cases with high doping ratio (HGB_H and VGB_H) are shown in Figures 1-34 through 1-38.

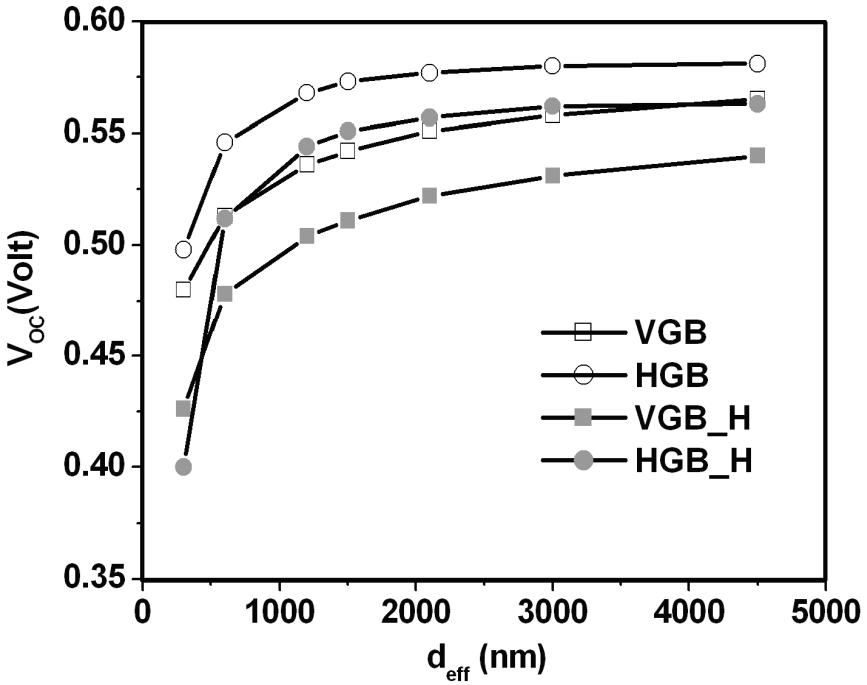

Figure 1-34. Effect of the depletion region width on the grain boundary orientation effect on V_{OC}.

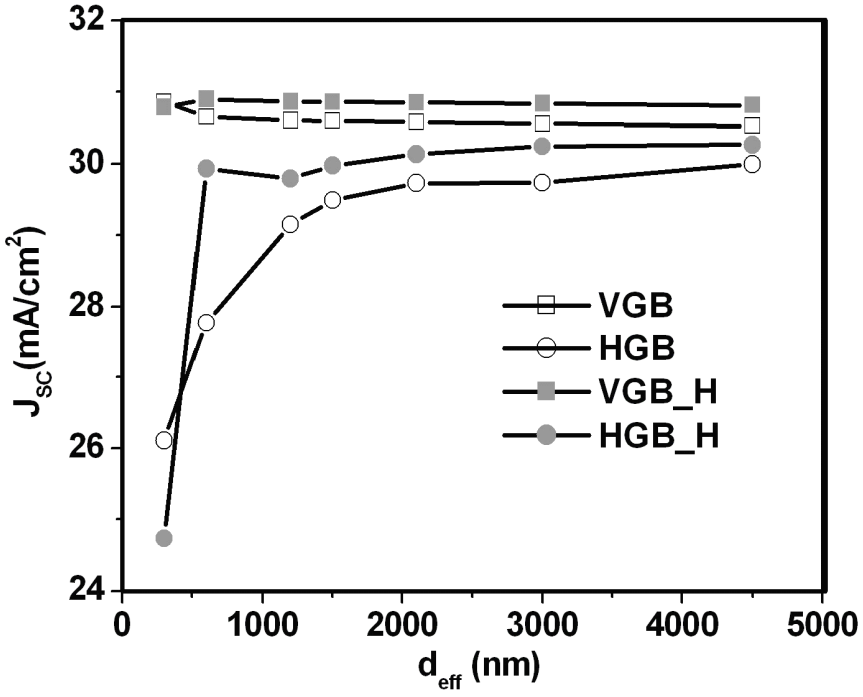

Figure 1-35. Effect of the depletion region width on the grain boundary orientation effect on J_{SC}.

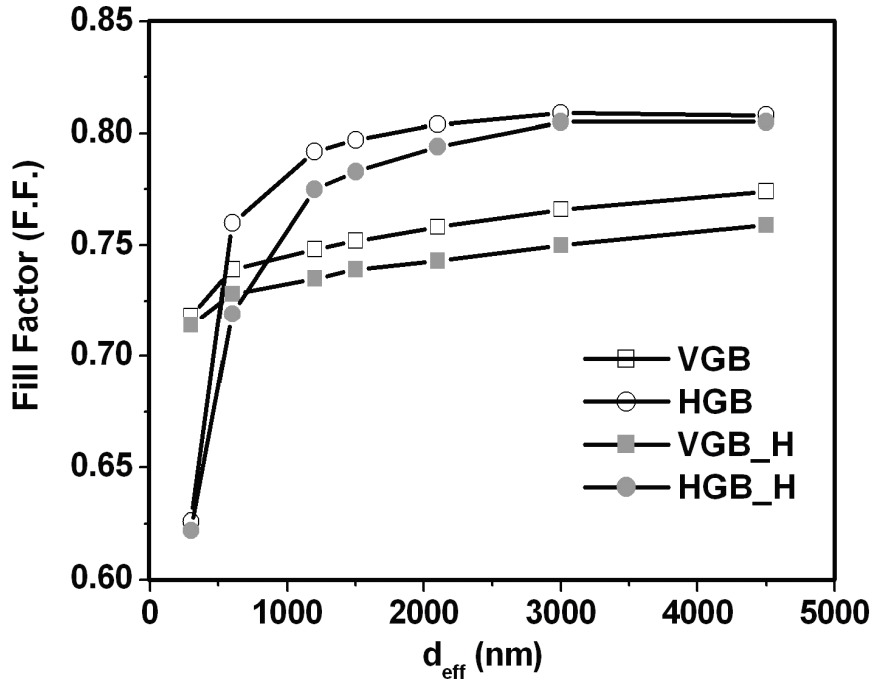

Figure 1-36. Effect of the depletion region width on the grain boundary orientation effect on F.F.

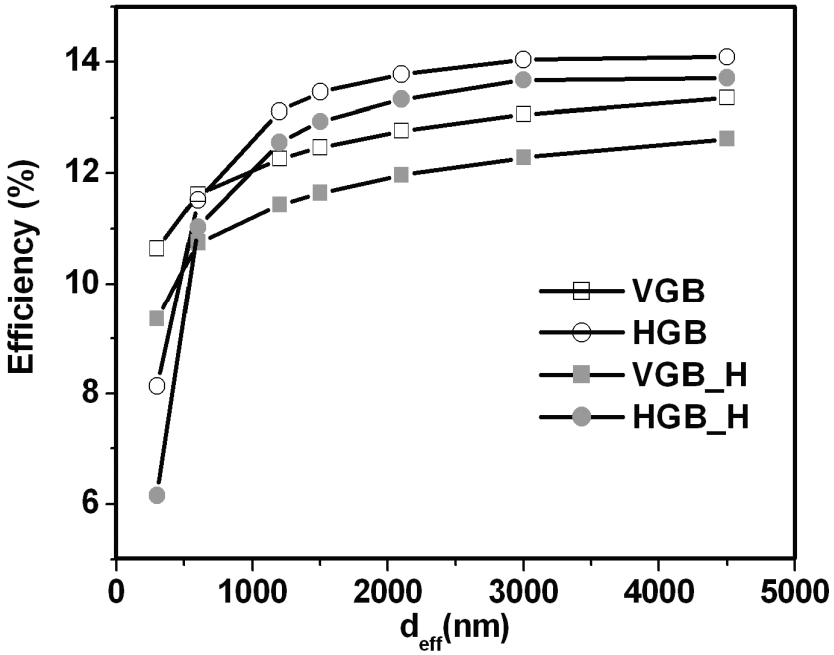

Figure 1-37. Effect of the depletion region width on the grain boundary orientation effect on η.

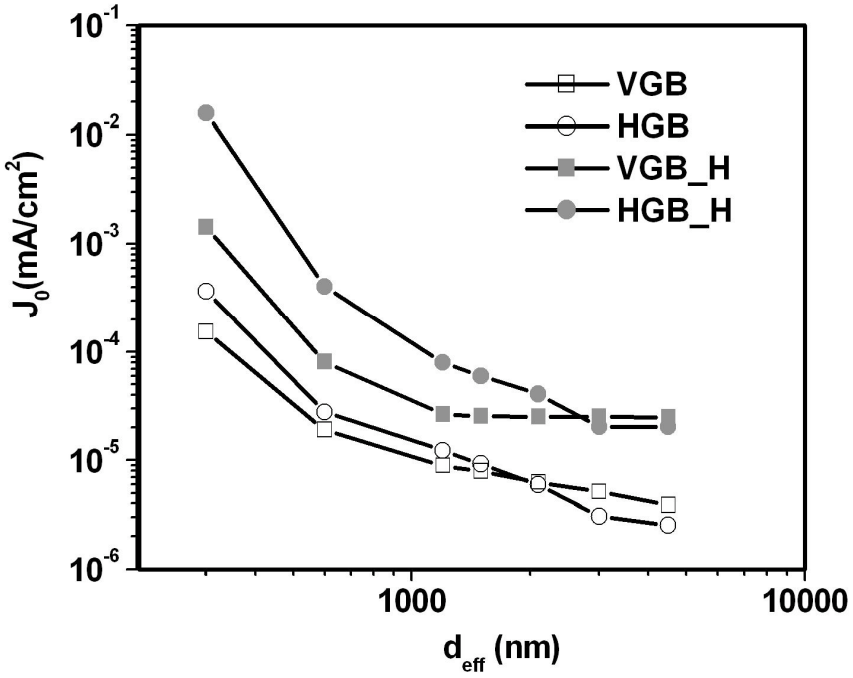

Figure 1-38. Effect of the depletion region width on the grain boundary orientation effect on J0.

Considering first the case of V_{OC}, it follows that for all grain sizes VGB_H shows lower V_{OC} than VGB. As shown in the calculation before, the length of the p-side depletion region is larger in the case of the higher doping ratio VGB_H than in VGB. Therefore, in the case of VGB_H more fractions of the vertical grain boundaries will be located in the junction depletion region, where the grain boundary effect is enhanced. While HGB shows higher V_{OC} values for all grain sizes in the case of the reference doping ratio, HGB_H shows lower V_{OC} values than that of VGB_H for the smallest grain size (d = 100 nm). As x_p for the case with high doping ratio was calculated as 186 nm, it is obvious that when the grain size is the smallest, the first grain boundary in CIS layer is completely located inside of the junction depletion region. Therefore, this behavior can be explained as the depletion region becomes larger enough to include one grain boundary in the case of HGB_H.

In the case of J_{SC}, the cases with the high doping ratio show the same behavior as the reference cases, which in turn showed lower values for the case of HGB due to the barrier effect to the transport of electrons. The values of J_{SC} for the high doping ratio cases, however, are larger than for the reference cases. This can be attributed to the lower doping level of the CIS layer (3.6×10^{16} cm^{-3}) compared to the reference-case doping level (6.6×10^{16} cm^{-3}). However, the J_{SC} of HGB_H shows smaller value than that of HGB when the grain size is 100 nm, and one grain boundary is completely included in the junction depletion region as shown in Table 1-6.

The cases with the high doping ratio show lower values of the efficiencies compared to the cases with the reference doping. This decrease in efficiency is mainly attributed to the decrease of V_{OC} that results from the reduction of the hole densities with more grain boundaries in the junction depletion region and the increased recombination. This increase of the recombination for the cases with high doping ratio (HGB_H, VGB_H) is also observed in the Figure 1-38 as both HGB_H and VGB_H show higher J_0 values than HGB and VGB, respectively.

1.5 Summary and Conclusions

The effect of grain boundaries on solar cell performance was investigated using two-dimensional simulation for a /ZnO/CdS/CIS/ cell structure. The influence of grain size and localized trap density was studied for square rectangular grain boundaries. The grain boundary was simulated by placing hole trap states at the grain boundaries. SRH recombination of trapped holes at grain boundary trap states with electrons was allowed, and the decrease of the minority carrier lifetime with decreasing grain size was also considered. The continuity and Poisson equations were solved self-consistently to determine the grain boundary potential as well as the Fermi-level at the grain boundary.

The calculation results indicate that the grain boundaries strongly influence V_{OC} through the trapping of holes. This drop on V_{OC} decreases the fill factor and the efficiency of the cell. If the grain size is smaller than a critical effective grain size, however, it appears that the entire region of the absorber layer becomes depleted and J_{SC} sharply decreases. The dark saturation current is also observed to increase with decreasing grain size. As the dark saturation current is composed of the recombination current and the diffusion current, this effect can be explained by the increasing recombination current due to the increase of effective trap density as well as the increase of the diffusion current from the reduced majority carrier density in the absorber layer.

From the dependence of dark saturation current, J_0, on the effective grain size, d_{eff}, two regions of J_0 were found to have a different carrier transport mechanism for the recombination of electrons with trapped holes at grain boundaries. For the grain size larger than the critical grain size, $d_{critical}$ (450 nm in this study) the diffusion of electrons to the edge of the depletion region determines the rate of recombination and the dark saturation current. In this case, J_0 is found to depend on $d_{eff}^{-1.5}$ from the scaling of the variables for J_0 and it agrees very well with the dependence of $J_0 \sim d_{eff}^{-1.53}$ obtained form the simulation results. For d_{eff} smaller than $d_{critical}$, it appears that the interior of the grain is completely depleted and the electric field in the grain and the grain boundary potential increases the rate of electron transport to the trap states at grain boundaries. Therefore, it is proposed that this change of electron transport mechanism gave the different dependence of J_0 on d_{eff}, $J_0 \sim d_{eff}^{-4.73}$, obtained from the simulation results. The critical grain size was also calculated from the plot of the net carrier density in the grain and the value, d_{eff} (300 ~ 450 nm) from the carrier distribution in the cell, shows good agreement with the value from the analysis of J_0. The decrease of grain boundary potential with light injection is observed only for cells with small grains. It is because, for large grain size, there are sufficient carriers to fill the traps (lower effective trap density) even without illumination. The increase of grain boundary potential with trap density at grain boundaries was observed and it indicates that as the trap density increases, the effective trap density increases, which results in the increase of filling probability of traps and the positive charge build-up at trap states.

The orientation of grain boundaries (VGB and HGB) has different effect on each performance parameter. The case, VGB shows lower V_{OC} values for all grain sizes. With the length of the depletion region of 88 nm in CIS layer, all grain boundaries in the case of HGB are outside of the junction depletion region while part of the grain boundaries are always in the junction depletion region in the case, VGB. The existence of grain boundaries in the junction depletion region results in the decrease of V_{OC} from the reduction of the carrier density since the recombination at grain boundaries is enhanced due to the electric field in junction depletion region.

Contrary to the effect of grain boundary orientation on V_{OC}, HGB shows lower J_{SC} values than VGB and decrease rapidly below the grain size of ~ 2000 nm while VGB shows no dependence on the grain size. It indicates that the horizontally oriented grain boundaries in the case of HGB act as the barriers to the transport of electrons that contribute to J_{SC}. Also, the rapid decrease of J_{SC} for small grain size can be explained as the decrease of electron density by the increased recombination.

For the efficiency and F.F., VGB shows lower efficiencies due to the decrease of V_{OC} with the enhanced grain boundary effect in the junction depletion region. For small grain sizes, HGB shows lower values both for the efficiency and fill factor than VGB as J_{SC} decreases rapidly with negligible differences of V_{OC} between VGB and HGB.

When the doping ratio of the CdS layer to the CIS layer increases, the length of the depletion region in the p-side CIS layer increases. With the increase length of the p-side depletion region (186 nm), HGB_H shows lower V_{OC} value than that of VGB_H for the smallest grain size (d = 100 nm) while HGB showed higher V_{OC} values for all grain sizes than VGB. It indicates that the junction depletion region can affect the grain boundary orientation effect when the depletion region width is large enough to include the whole horizontal grain boundary. In

other word, it appears that V_{OC} mainly depends on the fraction of the grain boundaries in the junction depletion region through the increased recombination.

For the cases with high doping ratio, J_{SC} shows the same behavior as in HGB and VGB, which means that HGB_H shows lower values of J_{SC} than VGB_H. The larger values of J_{SC} for HGB_H and VGB_H, however, than the reference cases is attributed to the fact that the doping level of the CIS layer (3.6×10^{16} cm^{-3}) is lower than that of CIS (6.6×10^{16} cm^{-3}) in the cases, HGB and VGB, which results in the increased minority carrier current. Also, the smaller value of J_{SC} in the case of HGB_H than the J_{SC} of HGB indicates that the complete inclusion of one horizontal grain boundary with the small grain size (100nm) resulted in the increased grain boundary effect in this case.

The lower efficiencies for the cases with the high doping ratio mainly result from the decreased V_{OC} due to the reduction of hole density than the reference doping ratio. It can be explained due to the increased recombination with more grain boundaries in the junction depletion region. The increase of the recombination current was also observed for the cases with high doping ratio (HGB_H, VGB_H) from the increase J_0 values and it indicates the increased recombination rate due to the more grain boundaries in the junction depletion region.

1.6 References cited

[1-1] K. Ramanathan, M.A. Contreras, C.L. Perkins, S. Asher, F.S. Hasoon, J. Keane, D. Young, M. Romero, W. Metzger, R. Noufi, and A. Duda, *Prog. Photovolt. Res. Appl.,* **11**, 225 (2003).

[1-2] W. Shockley, T. Read and R.N. Hall, *Phys. Rev. Lett.* **87**, 835 (1952).

[1-3] S.M. Sze, *Physics of Semiconductor Devices*, New York: Wiley & Sons, 1981, p. 790.

[1-4] J.A.M. Abushama, S. Johnston, R. Noufi, K. Ramanathan, G. Teeter, and T. Moriarty, *Prog. Photovolt. Res. Appl.***12**, 39 (2004).

[1-5] M.R. Murti, and K.V. Reddy, *J. Appl. Phys.* **70**, 3683 (1991).

[1-6] J. Palm, *J. Appl. Phys.* **74**, 1169 (1993).

[1-7] M. Kimura, S. Inoue, T. Shimoda, and T. Sameshima, *Jpn. J. Appl. Phys.*, **40**, L97 (2001).

[1-8] A.K. Ghosh, C. Fishman, and T. Feng, *J. Appl. Phys.* **51** (1), 446 (1980).

[1-9] Z. Chen, and L.C. Burton, *21st IEEE Photovoltaic Specialist Conference* 731 (1990).

[1-10] C. Wolfe, N. Holonyak, and G. Stillman, *Physical Properties of Semiconductors,*: Prentice Hall, 1989, Chapter 2.